

Contributions of TetrUSS to Project Orion

S. Naomi McMillin^{*}, Neal T. Frink[†]

NASA Langley Research Center, Hampton, Virginia 23681 USA

Johannes Kerimo[‡], Ejiaing Ding[‡], and Sudheer Nayani[§]

Analytical Services and Materials, Inc., Hampton, VA 23666 USA

and

Edward B. Parlette[¶]

ViGYAN, Inc., Hampton, VA 23666 USA

The NASA Constellation program has relied heavily on Computational Fluid Dynamics simulations for generating aerodynamic databases and design loads. The Orion Project focuses on the Orion Crew Module and the Orion Launch Abort Vehicle. NASA TetrUSS codes (GridTool/VGRID/USM3D) have been applied in a supporting role to the Crew Exploration Vehicle Aerosciences Project for investigating various aerodynamic sensitivities and supplementing the aerodynamic database. This paper provides an overview of the contributions from the TetrUSS team to the Project Orion Crew Module and Launch Abort Vehicle aerodynamics, along with selected examples to highlight the challenges encountered along the way. A brief description of geometries and tasks will be discussed followed by a description of the flow solution process that produced production level computational solutions. Four tasks conducted by the USM3D team will be discussed to show how USM3D provided aerodynamic data for inclusion in the Orion aero-database, contributed data for the build-up of aerodynamic uncertainties for the aero-database, and provided insight into the flow features about the Crew Module and the Launch Abort Vehicle.

Nomenclature

A – Area, sq. in.

A_l – rolling moment coefficient normalized by the rolling moment coefficient at $\alpha = 0^\circ$

A_n – yawing moment coefficient normalized by the yawing moment coefficient at $\alpha = 0^\circ$

A_y – side force coefficient normalized by the side force coefficient at $\alpha = 0^\circ$

C_A – axial force coefficient

C_D – drag coefficient

C_L – lift coefficient

C_m – pitching moment coefficient

C_N – normal force coefficient

C_p – pressure coefficient

CT – total coefficient of thrust for the Abort Motors

D – diameter of the Crew Module, inch

h – grid cell height, inch

log(R/R₀) – convergence parameter using the L2-norm solution residual of all flow variables

M, M_∞ – Mach number, freestream Mach number

MW – molecular weight

^{*} Research Aerospace Engineer, Configuration Aerodynamic Branch, Mail Stop 499

[†] Senior Aerospace Engineer, Configuration Aerodynamic Branch, Mail Stop 499, AIAA Associate Fellow

[‡] Senior Scientist, 107 Research Drive

[§] Senior Scientist, 107 Research Drive, AIAA Senior Member

[¶] Research Engineer, 30 Research Drive

Ncell – number of grid cells in a volume grid
 P, p – pressure, psf
 q – free-stream dynamic pressure, psf
 R – gas constant
 $R_{\text{universal}}$ – universal gas constant
 Re_D – Reynolds number based on the diameter of the Crew Module
 S_{ref} – reference area, $\pi D^2/4$, in.²
 T – temperature, °R
 TR – total thrust ratio for the Attitude Control Motors
 u – velocity component in the x axis, fps
 V – total velocity, fps
 v – velocity component in the y axis, fps
 w – velocity component in the z axis, fps
 X or x – streamwise coordinate, inch
 Y or y – spanwise coordinate, inch
 Z or z – vertical coordinate, inch
 α – angle of attack, deg.
 β – sideslip angle, deg.
 Δ – difference between two values
 ϕ – roll angle, deg.
 γ – ratio of specific heat for a gas
 ρ – density
 ∞ – free-stream condition

Subscripts:

air – air gas
 e – exit plane
 jet – jet gas
 t – throat plane
 tot – total conditions

Selected Abbreviations:

ACM – attitude control motor
 ALAS – alternate launch abort system
 AM – abort motor
 AR – analysis request
 ARSM – nonlinear Algebraic Reynolds Stress Model
 BPC – Boost Protection Cover
 BC – boundary condition
 CAP – CEV Aerosciences Project
 CEV – Crew Exploration Vehicle
 CFD Computational Fluid Dynamics
 CM – crew module
 DES – Detached Eddy Simulation
 IML – inner mold line
 IDAT – Integrated Design Analysis Team
 LAS – Launch Abort System
 LAV – Launch Abort Vehicle (Crew Module with Launch Abort System)
 PD – pressure dilation
 SA – Spalart-Allmaras one-equation turbulence model
 SCC – Sarkar compressibility correction
 SST – Menter Shear Stress Transport model
 TetrUSS - Tetrahedral Unstructured Software System
 WTT – wind tunnel testing
 k- ϵ – Jones-Launder linear two-equation turbulence model
 k- ω – Wilcox 1988 linear two-equation turbulence model

I. Introduction

NASA's Constellation program was initiated to address the needs of U.S. access to space in the post Space Shuttle era with the mission to the moon, Mars and beyond. Unlike the Space Shuttle, where both crew and cargo are launched simultaneously, the proposed architecture for the Constellation program included two separate launch vehicles: the Ares I crew launch vehicle and the Ares V heavy lift cargo vehicle. The Ares-I was to be the launch vehicle for the Orion Crew Exploration Vehicle (CEV) shown in Figure 1. The CEV consisted of 4 components which were the Launch Abort Tower (LAT), the Crew Module (CM), the Service Module, and the Spacecraft Adapter. The CM combined with the LAT comprises the Launch Abort Vehicle (LAV). While the Ares-I program has been canceled (including Ares I and Ares V), work is continuing on the Orion CEV. The intention is to mate them with a future launch vehicle.

The NASA Constellation program has relied heavily on Computational Fluid Dynamics (CFD) simulations for generating aerodynamic databases and design loads. The aerodynamic database development of the Orion CM and LAV is managed at NASA Johnson Spaceflight Center under the CEV Aerosciences Project (CAP) where multi-center coordination is provided for wind tunnel testing (WTT) and computational support.

The NASA Tetrahedral Unstructured Software System (TetrUSS) tool set¹ has served in a supporting role to CAP for investigating various aerodynamic sensitivities, such as WTT sting interference effects, WTT-to-Flight Reynolds number scaling with Abort Motors (AM), AM thrust offset, and Abort-Motor/Attitude-Control-Motor (AM/ACM) jet interactions. Each of these tasks required the delivery of hundreds of flow solutions with stringent data requirements and very tight time schedules. In the initial stages, TetrUSS, being a research tool, was not equipped for such demands and required urgent developments of new capabilities. The transformation of TetrUSS/USM3D from a research-oriented tool to a production-level tool in the midst of a fast-paced database generation campaign is described in Ref. 2. This paper will provide an overview of the contributions from the TetrUSS team to the Project Orion CEV and LAV aerodynamics, along with selected examples to highlight the challenges encountered along the way.

The paper is organized with a brief description of the CM and LAV geometries in Section II, followed by a brief overview of the TetrUSS system and capabilities in Section III. Section IV provides an overview of analysis requests that were assigned to the TetrUSS team, followed by Section V that describes the processes developed for producing production level computational solutions. Section VI describes the data used for comparison with four sample activities presented in Section VII. The Orion LAV and its aerodynamics have been designated sensitive but unclassified (SBU) due to export control restrictions under the International Traffic in Arms Regulations (ITAR). Therefore, to comply with SBU rules, some details have been removed from plots and figures in this paper.

II. Geometry Description

Several variations of the Orion CM and LAV configurations have been examined by USM3D. Figure 2 presents images of the Apollo CM and the Orion Integrated Design Analysis Team (IDAT) CM configurations. The Apollo CM had an apex cover whereas the Orion CM configurations did not. Figure 3 presents images of the 605-054 LAV and 606F LAV configurations. The Launch Abort Vehicle (LAV) is comprised of the CM inside the Boost Protection Cover (CM BPC) component of the LAT. The shoulder groove (see Fig. 3(c)) on the CM Base is not present in the early LAV configurations. Each nozzle has a jet boundary condition (BC) plane located far enough downstream of the nozzle throat that the inner nozzle wall is nearly conical from the jet BC plane to the jet exit plane (see Figs. 3(d-e)).

III. Computational Tools

TetrUSS was developed during 1990s to provide a rapid aerodynamic analysis and design capability to applied aerodynamicists. The system consists of component software for setting up geometric surface definitions (GridTool), generating tetrahedral grids (VGRID), computing Euler and Navier-Stokes flow solutions (USM3D), and extracting meaningful information from analysis of results (SimpleView). An overview of TetrUSS capabilities in early 2000 is presented in Ref. 1, with more recent enhancements in Ref. 2. A commercial tool for adapting tetrahedral grids to the flow solutions was also utilized to provide a key capability for the current work. The salient features of the tools are described below.

A. Grid Generation

VGRID^{3,4} is a tetrahedral grid generator based on the Advancing Front Method (AFM) for generation of surface triangles and 'inviscid' field cells, and the Advancing Layers Method (ALM) for generation of thin-layered 'viscous'

cells. Both techniques are based on marching processes in which tetrahedral cells grow from an initial front (triangular surface mesh) until the volume around the geometry is filled. Unlike the conventional AFM, which introduces cells into the field in a totally unstructured manner, the ALM generates organized layers of thin tetrahedral cells, one layer at a time, while maintaining the flexibility of AFM. Once the advancing front process is completed in VGRID, an additional post-processing step is required using POSTGRID to close any open pockets and to improve grid quality. VGRID input files are generated by an interactive geometry manipulation program, GridTool⁵. This graphics tool can import surface definitions from Initial Graphics Exchange Specification (IGES) files containing Non-Uniform Rational B-Spline (NURBS) surfaces and curves, as well as PLOT3D point definition files. GridTool is used to manipulate the geometry and to define necessary geometric surface patches and grid-spacing (source) parameters. It uses OpenGL for 3D graphics, and is available for Mac and Linux systems. The graphical interface is based on the Fast Light Toolkit.

B. Solution Adaptive Grids

Solution adaptive gridding was accomplished by the CraftTech CRISP CFD[®] code⁶. CRISP CFD[®] is a stand-alone tool for mesh modification and quality improvement of three-dimensional mixed-element unstructured meshes. Meshes comprised of tetrahedral, prismatic, and hexahedral regions may be readily modified to generate more accurate flow solutions through local refinement and coarsening. The adaption is driven by either an estimate of the solution error, or gradients of flow features. For tetrahedral cells as used in the present work, local refinement is achieved by means of a constrained Delaunay refinement algorithm combined with a circumcenter point placement strategy. Any inconsistency between the circumradius of a tetrahedron and some desired point spacing triggers the point insertion procedure. This iterative cell refinement is repeated until the cell circumradii are consistent with the prescribed point spacing. Coarsening of the tetrahedral region is also permitted through an edge collapse procedure. In regions where the grid is distorted or where solution errors are negligible, edges may be selected for removal. All cells incident to the deleted edge are removed from the mesh, the adjacent cells are redefined, and the two nodes of the edge are collapsed to a single vertex. Capability exists to modify the viscous layers of tetrahedral grids and underlying surface mesh. However, initial experience led to only adapting in the inviscid region of the grid at this time.

C. Flow Solver

USM3D^{7,8} is a parallelized tetrahedral cell-centered, finite volume compressible Reynolds-Averaged Navier-Stokes (RANS) flow solver. The term “cell centered” means that the finite volume flow solution is solved at the centroid of each tetrahedral cell. Inviscid flux quantities are computed across each tetrahedral cell face using various upwind schemes. Spatial discretization is accomplished by a novel reconstruction process, based on an analytical formulation for computing solution gradients within tetrahedral cells. The solution can be advanced in time by a 2nd-order “physical” time step scheme, a 2nd-order “dual” time step scheme, or to a steady-state condition by an implicit backward-Euler scheme. Several turbulence models are available: the one-equation Spalart-Allmaras (SA) model, and the linear two-equation k - ϵ model by Jones and Launder, the Wilcox 1988 linear two-equation k - ω model, the Menter Shear Stress Transport (SST) model, and the two nonlinear Algebraic Reynolds Stress Models (ARSM) of Girimaji and Shih/Zhu/Lumley. Detached Eddy Simulation (DES) has been implemented in all of the turbulence models. A capability to trip the flow at specified locations on aerodynamic surfaces has been implemented for the k - ϵ turbulence model, but fully turbulent flow is assumed for the results in this paper. USM3D also has capabilities for overset grids and dynamic grid motion, which are not utilized in the current work.

IV. Summary of CAP Task Requests

The requests by the CAP office at NASA Johnson Space Center for computational support from the TetrUSS team are chronicled in Table 1. The list contains an identifier for each task, the subject geometry, a descriptive title, and its main objective. The majority of the analysis requests (AR) was directed toward various configurations of the LAV. Table 2 contains the corresponding flow conditions, jet conditions, grid information, and date of the tasks. Note the majority of the data were generated at transonic and low supersonic speeds. The tasks covered multiple objectives such as adding data to the project’s aerodynamic database, calculating WTT sting interference increments, evaluating WTT-to-Flight Reynolds number scaling with the AMs firing, determining effects of the AM thrust offset, and investigating AM/ACM jet interactions.

V. Flow Solution Process

The process for applying TetrUSS/USM3D toward generating accurate Navier-Stokes solutions with quantifiable uncertainty has evolved over the five years of supporting the Orion Project. Table 3 contains the flow solution process. The process is split into 3 stages: USM3D input stage (step 1), grid generation stage (steps 2-6), and convergence stage (steps 7-9). Steps 1-2 of Table 3 are conducted on a local computational platform whereas the remaining steps were conducted on the NASA Advanced Supercomputing (NAS) Columbia Altix cluster. Steps 4-8 are controlled by shell scripts. The adaptive grid utility CRISP CFD[®] version 1.5.1⁹ was run on a single processor while the remaining steps were conducted on 128 processors. Step 9 is completed manually. More details of the steps are provided below.

A. USM3D Input Stage

This section describes the current USM3D input strategy, which has evolved from several guideline studies and extensive application. Reference 10 contains more details on the various input files and techniques.

1. Flow, Geometry, and Code Input

Flow conditions (Mach number, Reynolds number, temperature, etc) and geometry conditions (i.e. angle of attack, reference area, etc) were specified in the “*project.inpt*” file for USM3D. Various code parameters, e.g. time step, flux scheme, under-relaxation factor, etc., were also controlled through this file.

Flow re-initialization of selected user-prescribed volume cells was often used to alter default freestream conditions and enable more robust solution startup. This feature greatly improves the robustness of startup from freestream flow by re-initializing the cells within the high-pressure AM and ACM nozzles of the LAV, or in the subsonic pocket behind the CM Base embedded within a supersonic free-stream.

During the guideline studies listed in Table 1, parametric studies were conducted on the available turbulence models in USM3D. For the tasks after Guideline Study 3 in Table 1, the SST turbulence model with the Sarkar compressibility correction (SCC) and pressure dilation (PD) was selected after statistical analysis of correlations with experimental wind tunnel data¹⁰. All computations were performed with the assumption of fully turbulent flow. Because of the very tight time schedules, virtually all runs were made “steady-state” with local time-stepping convergence acceleration. An occasional time-accurate solution was conducted when unsteady flow effects were significant.

2. General Boundary Conditions

The boundary conditions for the geometry surfaces and outer grid boundary were set in the “*project.mapbc*” input file that lists all of the surfaces of the grid. The outer boundaries of the grid were set to characteristic inflow/outflow condition. The surface boundaries of the vehicle were set to a no-slip BC except for the inner-mold-line (IML) surfaces of the ACM and AM nozzles. For jets-off conditions, the jet BC plane and the IML nozzle walls were set to a viscous boundary condition. For jets-on conditions, the jet BC plane has a boundary condition described in the next section and the IML nozzle walls were set to an inviscid boundary condition. If present, the sting surface was set to an inviscid tangent flow boundary condition.

3. Jet Inflow Boundary Conditions

The jet BCs for the AM and ACM nozzles were derived using the wind tunnel flow conditions or flight LAV trajectory data depending on the configuration and objective. Mach number (M), pressure (P), and density (ρ) were computed at the nozzle exits, then extrapolated using isentropic relationships to a jet BC plane located slightly downstream of the nozzle throat using isentropic relationships. The Appendix describes the equations and process used to calculate the jet BCs. The jet BCs were input to USM3D through the “*project.jetbc*” file. The velocity vectors on the recessed jet were “fanned” across the surface from the center nozzle axis until becoming tangent at the nozzle walls. No attempt was made to simulate the boundary layer of the jet inflow, thus a tangent flow “inviscid” BC was applied to the nozzle IML to improve numerical stability.

The current USM3D code is limited to ideal gas with air, without a capability for modeling multiple species gases to simulate the chemical composition of the AM and ACM plumes characteristic of the flight vehicle. Hence the hot jet simulations are constrained to air with the ratio of specific heat of $\gamma_{\text{air}} = 1.4$ and a gas constant of $R_{\text{air}} = 1716.47$. This assumption is reasonable for comparing with cold-jet wind-tunnel nozzle configurations. For the hot-jet USM3D simulations, the jet BC values for the non-air gas conditions(i.e. γ_{jet} and R_{jet}) are corrected from a non-air gas to air as described in the Appendix. The advantage of this type of correction for γ and R is that it duplicates the true jet gas exit pressure - an important parameter in jet exhaust expansion and therefore plume shape. It also

duplicates the jet mass flow and exit velocity, both important parameters for entrainment and for maintaining desired levels of the thrust.

B. Grid Generation Stage

The grid generation process continually evolved as configuration geometries became more complex and high-powered jet plumes added new requirements for grid resolution. The following describes the range of techniques employed to deliver the required solutions on schedule.

1. Base Grids

The base tetrahedral grids (i.e. unadapted grids) were generated using the VGRID4.0 code⁴. Several configurations examined included wind tunnel stings. However, wind tunnel walls were never modeled. Full configuration tetrahedral grids were produced with an outer boundary box prescribed at minimum x, y, z of, at least -100D, -100D, -100D, respectively, and maximum x, y, z of, at least, 100D, 100D, and 100D, respectively, where D is the CM diameter. The grids were verified to have an average y-plus of 0.25 at the centroid of the surface tetrahedra. This parameter was mostly dependent on Re_D . Thus for a common geometry, wind tunnel Re_D conditions would have a different grid than those of flight Re_D conditions. In the first year of the USM3D work, the base grid was used for the unpowered LAV configurations.

2. Predefined Wake Grids

The initial computations on a base grid for the Apollo CM exposed the critical need for grid refinement of the grid in the wake region.¹¹ This observation presented a considerable operational challenge since a large number of angles of attack (α) were computed between 0° and 180° with each requiring a unique grid refinement. To solve this problem, an h-refinement utility was applied in a four-staged process to progressively refine smaller and smaller sub-regions as illustrated in Fig. 4. Figure 5 presents several grids for the Apollo CM of Guideline Study 1¹¹ of Table 1. Figure 5(a) presents the four successive grids generated in the predefined wake grid generation process for $\alpha = 0^\circ$. The directional refinement observed in Figs. 5(b-c) was generated automatically using a script for $\alpha = 40^\circ$ and 150° , respectively. The script performs the proper user-prescribed rotations and successive subdivisions of the grid within the cone regions.

3. Solution Adapted Grids

As the CAP tasks became more focused on the LAV, grids became more difficult to generate due to increased geometric complexity and the challenge of volumetric grid refinement for components such as the AM and ACM plumes, and the cross-flow wake behind the tower and CM BPC. Several of the earlier tasks for the unpowered LAV (up to AR-60 in Table 2) were conducted with no adaption of the base grid. The eventual inclusion of powered jets, beginning with AR-76¹², drove the firm requirement for solution adaptive grids to resolve the features and interactions of the AM and ACM plumes as illustrated in Fig. 6 for the 606F LAV configuration. Figure 6 presents results for the preliminary solution on the base grid at $M_\infty = 1.1$, $\alpha = 5.0^\circ$, $Re_D = 64.4 \times 10^6$, a combined AM thrust coefficient (CT) of 4.0 for all 4 AM nozzles, and a combined thrust ratio (TR) of 0.04 for the two south-firing ACM nozzles[#]. Figure 6 shows data on a streamwise plane cutting through the AM nozzle that is offset from the symmetry plane by a roll angle (ϕ) of 45° . The grids and Mach contour data (on the $\phi = 45^\circ$ plane) are shown around the shaded LAV surfaces. The base grid and the Mach contour data from the preliminary solution are shown in Fig. 6(a). The upper value of Mach number is clipped to a less than maximum level to enhance the details of the plume interactions with the aerodynamic surfaces, which results in the inner portion of the jet plume being solid red. The adapted grid based on the preliminary solution is shown in Fig. 6(b). The adapted grid is shown on top of the Mach contour data on the right side of Fig. 6(b). The clustering of adapted cells is evident in the AM and ACM plumes, around the shoulder of the CM BPC, and within the wake region of the CM Base.

More detail of the 606F LAV grid is shown in Fig. 7. A layer of viscous cells near the surface exhibits large disparities in cell size relative to the adjacent adapted cells. This is an artifact of the CRISP CFD[®] code that only creates isotropic tetrahedra for the adapted cells. CRISP CFD[®] has the capability of adapting through the viscous layers, but has shortcomings with the surface grid adaption. The effect of adapting through the boundary layer was investigated and was determined to be negligible to overall force and moment values. Note the near absence of viscous layers at the intersection of the lower tower and fairing. The thickness of this layer is based on the relative size of the surface triangle compared to the nearby inviscid spacing – the smaller the surface cell size the thinner the viscous layer.

[#] A discussion of the ACM jet firing orientation can be found in Ref. 13.

The length (as defined by number of iterations) of the preliminary solution, which was used to adapt the base grid, has evolved. For AR-76 through AR-105 the preliminary solution was a 1st-order base-grid solution of approximately 3,000 iterations. From AR-112 to AR-128 the preliminary solution was allowed to progress to a 2nd-order base-grid solution of approximately 15000 iterations. Figure 8 shows the coefficient convergence history of C_A for two solutions that varied by the length of the preliminary solution used to derive the adapted grid. The solutions are for the 606F LAV configuration at $M_\infty = 1.1$, $\alpha = 0^\circ$, $Re_D = 64.4 \times 10^6$, a combined CT = 3.0 for the four AM nozzles, and a combined TR = 0.04 for the two south-firing ACM nozzles. C_A has a discontinuity where the solution switches from 1st order to 2nd order and at the restart on the newly generated adapted grid. The solution on the left of Fig. 8 had a preliminary solution of 3000 iterations and was a 1st-order solution (referred to hereafter as the I=3000 solution). The solution on the right of Fig. 8 had a preliminary solution of 15,000 iterations and was a second order solution (referred to hereafter as the I=15000 solution).

Figure 9 presents Mach contour and adapted grid data from the preliminary I=3000 and I=15000 solutions of Fig. 8. The Mach contour data of the I=3000 solution are shown on the left side of Fig. 9 and the data of the I=15000 solution are shown on the right side of Fig. 9. Beneath each Mach contour is the grid that was adapted using the solution at that iteration. Three different cross-sectional views are shown in Fig. 9. The two solutions show differences in the Mach contour data such as:

- AM plume sits on the shoulder of the CM BPC for the I=3000 solution but has lifted off that shoulder for the I=15000 solution (see Fig. 9(a))
- a shock on the upper surface of the upper tower is further downstream for the I=15000 solution than in the I=3000 solution (see Fig. 9(b)).
- ACM plumes are more symmetric for the I=3000 solution than for the I=15000 solution (see Fig. 9(c)).

The above differing flow structures yielded slightly different adapted grids as seen in the accompanying adapted grid images of Fig. 9. These slightly different grids produce different convergence behavior as seen in Fig. 8. The I=15000 solution has asymmetric ACM plumes but C_A levels out better than that of the symmetric ACM plumes of the I=3000 solution.

C. Convergence Stage

The aerodynamic force and moment coefficients were extracted as an average of the last 1000 solution iterations. Thus, quantitative characteristics of the evolving behavior for these coefficients as the flow solution develops provide a numerical approach to determining convergence. Once an adapted grid was generated and initialized with the base-grid flow solution, the convergence stage (steps 7-9 of Table 3) began. After an additional 8000 iterations on the adapted grid, an automated monitoring script checked the USM3D output in 15-minute intervals to determine if the convergence criteria listed in Table 4 were met. When two of the first three criteria were met, the solution was automatically stopped. The last step of the run process required the user to examine a solution summary chart, and other data if necessary. If the user decided that more iterations were necessary to further the convergence of the solution, the solution was restarted and step 8 in Table 3 was repeated for a user-defined number of iterations. In cases where the solution fails, deviation from the default process was required. More details about the troubleshooting process are given in Ref. 10.

Once the monitoring script of Step 8 in Table 3 stopped the solution, the user examined the solution using a solution summary chart. A representative solution summary chart is presented in Fig. 10 for the unpowered ALAS11r3b configuration at $M_\infty = 1.3$, $\alpha = -8^\circ$, and $Re_D = 2.5 \times 10^6$ at solution iteration 9,398. The right side of the summary chart displays flow Mach contour data on a streamwise plane cutting through the AM nozzle that is offset from the symmetry plane by a roll angle of 45° . In the lower right corner of the chart is a plot of the surface pressure coefficient (C_p) contours with a longitudinal cutting plane through the AM nozzles depicting Mach contour data of the jets. The left side of the summary chart tracks the convergence history of the solution. The lower left plot in Fig. 10 depicts the history of the order-of-magnitude drop of the L2 residual norm of the conservation equations (five flow variables) and the upper left plot depicts the histories of the axial force coefficient (C_A), normal force coefficient (C_N), and pitching moment coefficient (C_m) for the nose-to-base configuration. The IML and jet BC plane for each motor and the sting were excluded from integration of the three coefficients shown in Fig. 10.

The solution shown in Fig. 10 meets convergence criteria 1 and 2 at iteration 9,398. However, the delta of the maximum and minimum of C_A over the last 1000 iteration is greater than the tolerance of 0.004 and thus criterion 3 is not met. A visual inspection of Fig. 10 shows that C_A has not achieved convergence, although the percentage requirement of 1% variation in criteria 1 and 2 are met due to the relatively large magnitude C_A . Therefore a 5th criterion was imposed on such cases. The 5th criterion required that the absolute value of the delta between coefficients averages at the two iteration intervals be less than 0.002. The solution of Fig. 10 was extended until this

5th criterion was met at iteration 11,219 as shown in Fig. 11 where the C_A convergence history levels off to within tolerance. About half of the solutions met two of the first three criteria but still did not appear converged upon visual examination of the convergence history. These solutions were extended until the 5th criterion was met.

Five different classifications of convergence history were observed in the USM3D tasks. The five types presented in Fig. 12 are: normal, oscillation, small oscillation, irregular oscillation, and curve break convergence. The type of convergence could sometimes affect the final aerodynamic coefficient averages from a solution. For example, a solution with a regular periodic oscillation in one or more aerodynamic coefficients with respect to iteration was considered to have an oscillation convergence (see Fig. 12(b)). Usually, the oscillating coefficients had two or more cycles in the last 1000 iterations such that the average taken over the last 1000 iterations was deemed acceptable. However, if less than two cycles occurred during the last 1000 iterations, a new interval of iterations based on the last two cycles would be used to calculate the averages and to re-compute the convergence criteria. The irregular oscillation convergence had no regular cycle in the oscillations (see Fig. 12(d)). The small oscillation convergence type (see Fig. 12(c)) was similar to the oscillation convergence type with a much smaller oscillation magnitude. The irregular oscillation and small oscillation convergence types had a coefficient oscillation less than 0.004 and thus retained the 1000 iteration interval for calculating averages and convergence criteria. The curve break convergence type in Fig. 12(e) occurred with a sudden shift in the coefficient history, usually when a major shift in the flow structure developed in the evolving solution. Just before the break in the coefficient vs. iteration curve the convergence appeared normal and very close to satisfying the convergence criteria. After a sudden shift in the coefficient history the solution was allowed to run further until the convergence criteria is met. The curve break convergence type is not a common type. For AR-105, 11 of the 230 cases performed had the curve break convergence and 10 of those were at $M_\infty = 1.1$ and 1.3. The 11th case occurred at $M_\infty = 2.0$

VI. Comparison Data

The USM3D results are compared with Project Orion data obtained from three sources. The first is experimental data from the various wind tunnel tests within the project. These tests provided force and moment measurements as well as limited surface pressure data. In the latter stages of the project, some pressure sensitive paint data were obtained but are yet to be compared with USM3D results. The second source of comparison data is from the *Orion Aerodynamic Databook*¹⁴ which contains data also called the Orion aero-database. The aero-database is the project's best estimate for the aerodynamics vehicle shown in Fig. 1. The aero-database is based on available experimental and computational data and has evolved as additional data are developed (including the USM3D tasks). The third source of comparison data is computational results from the OVERFLOW¹⁵ structured-grid code which is producing large amounts of data to the Orion project.

VII. Sample Applications

Over the course of the Orion CAP Project, TetrUSS/USM3D has provided an extensive amount of computational aerodynamic and loads data on two types of configurations – the solitary CM and the LAV (with and without the AMs and ACMs firing). Approximately 500 solutions were obtained for CM configurations, 400 solutions for unpowered LAV configurations, and 1,100 solutions for powered LAV configurations. The following describes some typical results from the TetrUSS/USM3D tasks and their impact to the project.

A. Apollo CM Configuration

An initial guideline study was conducted on the Apollo CM to develop the practices for generating the static aerodynamic coefficients on CM configurations at transonic and low supersonic M_∞ (i.e., $0.7 \leq M_\infty \leq 2.4$). The practices were determined through systematic parameter studies of grid resolution, turbulence models, flux schemes, limiters, etc. The turbulence models that were considered are the Spalart-Allmaras (SA) model, the linear k- ϵ model, the Girimaji nonlinear k- ϵ model, and the Menter Shear Stress Transport (SST) model. The effect of turbulence model is examined in Fig. 13 for the Apollo CM configuration at $M_\infty = 0.9$, wind tunnel R_D , and $0^\circ \leq \alpha \leq 180^\circ$. The aerodynamic coefficients were calculated as the average over the last 1000 iterations. As observed in Fig. 13, no clear guidance is apparent regarding the selection of a superior turbulence model for the Apollo CM aerodynamics, illustrating the complexity of the flow field around such a benign geometry. Models that correlate well at one end of the α -range do not correlate as well at the other end of the range. From this study, both the linear and non-linear k- ϵ models were eliminated due to lack of robustness. Hence, the SA and SST models were retained for future calculations on the CM geometry.

Fig. 14 presents the Mach contour data on the $Y = 0''$ cutting plane for twelve angles of attack. These images provide insight into the dominant flow mechanisms that induce the aerodynamic behavior. For example, the lower and higher angles of attack are dominated by pure blunt-base flows, whereas the mid-range angles ($60^\circ \leq \alpha \leq 80^\circ$) experience a strong influence from smooth round surface cross-body flow separation, which is very difficult to model. The sensitivities in the mid-range are even evident as large differences in the experimental data presented in Fig. 13. Thus, one should expect any numerical prediction of aerodynamics for $60^\circ \leq \alpha \leq 80^\circ$ to have large uncertainties.

The variations in coefficients due to the different turbulence models were used in developing aero-database uncertainties. The CM simulation guidelines developed here were used to produce a full set of solutions on the CEV CM that were incorporated into the Orion aero-database. These guidelines also provided a starting point for the LAV guidelines.

B. IDAT CM Configuration

The IDAT CM configuration shown in Fig. 2 was examined in AR-122 of Table 1 to generate data for the most recent CM aerodynamic database. A small study was performed initially to refine the application guidelines. This task required a combination of predefined wake grids (used in the above sample) with additional adaptation of the flow solution. A base grid was first generated with a predefined cell clustering in the wake region at a prescribed angle of attack, and then CRISP CFD[®] was applied to further adapt the grid to the flow solution. Each angle of attack had a uniquely defined wake region. Figure 15(a) presents the baseline base grid and the baseline adapted grid for the CM at $M_\infty = 0.5$ and $\alpha = 150^\circ$. Preliminary solutions on the IDAT CM indicated a strong sensitivity to the grid resolution around the CM shoulders. Therefore, a finer base grid was generated with additional clustering around the shoulders (see Fig. 15(b)).

The USM3D aerodynamic coefficients (C_A , C_N , and C_m) are correlated with OVERFLOW data and the IDAT CM aerodynamic database Version 0.55 in Fig. 16 for $M_\infty = 0.5$ at $135^\circ \leq \alpha \leq 160^\circ$. OVERFLOW predicts a break in the C_A vs. α curve between $\alpha = 150^\circ$ and $\alpha = 155^\circ$. Both steady state and time-accurate USM3D solutions are presented in Fig. 16 for the baseline and finer grids. The steady-state USM3D solutions do not predict, with either grid, the break in the C_A vs. α curve observed in the OVERFLOW time-accurate solution. Also the increment in C_A between the baseline and finer grids is nearly constant over the α -range. In contrast, the increment in C_N and C_m due to grid resolution is significant and increases with decreasing angle of attack for the α -range shown in Fig. 16. Outside of $135^\circ \leq \alpha \leq 160^\circ$ range, USM3D data agrees better with the OVERFLOW data (not shown here).

Figure 17 presents Mach contour and surface pressure coefficient (C_p) contour data at $\alpha = 150^\circ$ for both the baseline and finer grids. The lower surface of the CM body has a lower C_p for the baseline grid solution which produces a higher C_N and lower C_m at $\alpha = 150^\circ$. The data of Fig. 17 represent the last iteration of a slightly oscillatory convergence. An examination of Mach and C_p contours at several prior iterations verified that the observed behavior is not significantly changed. The variation in the coefficients' oscillating convergence histories is due to small increases and decreases in the low C_p data observed above.

The convergence histories for the baseline and finer grids are presented in Fig. 18 for $\alpha = 150^\circ$. The steady-state solution is evident prior to the notation of the time-accurate solution in the figure. The time-accurate solutions were started from an iteration where the steady-state solutions were considered converged according to the criteria in Table 4. C_A for the time-accurate solutions oscillates by approximately ± 0.02 whereas C_N and C_m settled to within ± 0.003 . Figure 19(a) presents the Mach contour data on the $Y = 0''$ plane for the finer-grid time-accurate solution at four time steps representative of two cycles of C_N oscillation. In contrast to the steady solution (shown in Fig. 17), the wake in the time-accurate solution is highly oscillatory. The corresponding impact on the surface C_p contours on the conical shell of the CM is presented in Fig. 19(b) as viewed from the front of the CM. Significant variation of C_p with time is observed and could easily alter the interplay of forces that result in the breaks in coefficients of the time-accurate solutions in Fig. 16.

To summarize, USM3D predictions, at these conditions, are sensitive to grid resolution, are predicting an unsteady flow about the IDAT CM, and do not compare well with OVERFLOW or aero-database results in the range of $135^\circ \leq \alpha \leq 160^\circ$. These results indicate a need for experimental data to better quantify the aerodynamics in range of $135^\circ \leq \alpha \leq 160^\circ$. The USM3D IDAT CM results were used in defining uncertainties for the aero-database.

C. 19-AA LAV Configuration

Task AR-41¹⁶ was initiated to provide supporting computational aerodynamic analysis of perceived WTT data anomalies and sting interference effects for the 19-AA LAV wind tunnel model. The 19-AA LAV model was based

on the LAV 605-054 PA-1 geometry but had a slightly longer upper tower. The 19-AA LAV model was tested at the Boeing Polysonic facility in St. Louis, Missouri. In order to completely cover the desired α -range of 0° to 180° , five different sting configurations were tested as presented in Fig. 20. Each sting had a different α -range as noted in Fig. 20 with overlaps occurring. No testing occurred at $130^\circ < \alpha < 140^\circ$. Grids were generated using VGRID with no grid adaption. A sixth configuration with no support sting was added to the USM3D task and is referred to as the free-air configuration.

Aerodynamic data over the full range of angle-of-attack at $M_\infty = 0.5$, constructed from measurements using a composite of the five sting configurations, are presented in Fig. 21. The experimental data for the 5 different stings were plotted as solid lines in different colors. For example, measurements at $\alpha = 30^\circ$ were made with both the 15° sting (red) and the 50° sting (green). Similarly the data at $\alpha = 60^\circ$ and 70° reflect dual measurements from the 50° sting (green) and the 77.5° sting (blue). It is observed for C_A , C_N , and C_m that the trends of the sting effect on the coefficients are consistent in the sting overlap regions between the USM3D solutions and the wind tunnel data, although the magnitudes are not always comparable. Such trends for sting effect are not fully consistent with C_m as evident at $\alpha = 60^\circ$, 70° , and 95° . Sting-interference corrections relative to the free-air configuration were provided to the CAP team and incorporated into the aero-database for unpowered LAV flight.

D. 606F LAV Configuration with ACMs and AMs Firing

USM3D has primarily served as a second computational data source to the CAP team for supplementing the primary data computed with the OVERFLOW code. The objective for AR-112 in Table 1 was to provide data for assessing jet interference effects from the AM and ACM plumes on the LAV Fairing and CM BPC. Midway through the task, an additional focus was added to examine a flow asymmetry issue that was discovered during a parallel OVERFLOW task. During the OVERFLOW study, abnormal asymmetries were discovered in the ACM plumes at certain flight conditions for cases with symmetric jet conditions and a near symmetric geometry. Figure 3(b) presents sketches of the 606F LAV configuration for which the LAV/Service Module umbilical cavity is offset to the left of the LAV centerline.

A short grid study was conducted to determine the sensitivity of AM/ACM interactions to grid resolution. One result from this study was the use of a longer, second-order solution more fully converged for the grid adaption as was discussed previously for Fig. 9. Figure 22 presents another aspect of the grid study – the use of a predefined cone grid on the upper tower. The baseline base grid and the base grid with a predefined cone grid (referred to as the predefined-cone base grid) are presented at two cross-section cuts in Fig. 22. Note that the predefined cone grid (on the left of Fig. 22) on the upper tower stopped just ahead of the AMs.

Figure 23 presents the adapted grids and Mach contour data generated for the baseline and predefined-cone grids at $M_\infty = 1.1$, $\alpha = 10^\circ$, a combined CT = 3.0 for the four AM nozzles, and TR = 0.04 for the two south-firing ACM nozzles. Figure 23(a) shows a denser cluster of cells about the upper tower for the predefined-cone grid. Details of the grid about the ACM plumes is seen in Figs. 23(b-d). Both the baseline and predefined-cone grids predict asymmetric ACM plumes. However, the asymmetry changes sides as clearly seen in Fig. 23(d) - Station A on the upper tower for the finer predefined-cone grid. The asymmetry switch is apparent in comparing the adapted grid views on the $\phi = 22.5^\circ$ and -22.5° planes (see Figs. 23(b-c)). The impact of the asymmetry present between the two ACMs is also evident in the Mach contour data at the Station B cross-section (see Figs. 23(e-f)) which occurs downstream of the AMs.

Figure 24 presents the coefficient data for the OVERFLOW and USM3D solutions at $M_\infty = 1.1$, $-10^\circ \leq \alpha \leq 10^\circ$, a combined CT = 3.0 for the four AM nozzles, and TR = 0.04 for the two south-firing ACM nozzles. USM3D data from both the baseline and predefined-cone base grids of Fig. 22 are presented. As seen in Fig. 24(a), USM3D underpredicts C_A when compared to OVERFLOW. C_N and C_m data have a better comparison at $\alpha \leq 0^\circ$. The USM3D C_A , C_N , and C_m data for both grids show little variation between the baseline grid and the finer predefined-cone grid (excepting the $\alpha = -5^\circ$ case).

The lateral-directional coefficients of Fig. 24(b) have been normalized by dividing each coefficient with the absolute value of that coefficient on the USM3D baseline grid at $\alpha = 0^\circ$ which was non-zero. Using the absolute value at $\alpha = 0^\circ$, the asymmetry, as reflected by the sign of the coefficient, is retained. For both USM3D and OVERFLOW, the normalized C_Y (known as A_Y) data show asymmetric flow (i.e. A_Y is not equal to zero) at various α /CT/TR conditions. For example, at $\alpha = 10^\circ$, USM3D predicts asymmetric flow, i.e. $A_Y > 0.0$ for the baseline grid which corresponds to the asymmetric jet plumes seen in the Mach contour data of Figs. 23(b-d). Also note that USM3D predicts a change in asymmetry between the USM3D baseline grid and the USM3D predefined-cone grid

as noted by a change in the sign of A_Y between the two solutions. The Mach contour data of Fig. 23(d) shows a corresponding switch in the jet plume asymmetry for the $\alpha = 10^\circ$ case.

The A_Y data of Fig. 24(b) also show a change in angle of attack can trigger a switch in asymmetry. For example, OVERFLOW and USM3D both predict a change in asymmetry between the $\alpha = 0^\circ$ and $\alpha = 5^\circ$ conditions. Fig. 25 presents the Mach contour data at the Station A cross-section on the upper tower for both USM3D grids at all five angles of attack. The USM3D predefined-cone grid solution predicts a switch in the large jet plume from the left to the right side at a change in angle of attack of 0° to 5° that corresponds to a change in sign for A_Y . However, the jet plume does not switch sides between $\alpha = 0^\circ$ and $\alpha = 5^\circ$ on the baseline grid. In fact at $\alpha = 0^\circ$ the baseline and predefined-cone grid solutions have nearly equal values in A_Y while having the large jet plume appearing on opposite sides. Figure 26 presents a bar graph of A_Y for each component of the nose-to-base geometry from both grids' solutions at $\alpha = 0^\circ$. A_Y for the total nose-to-base geometry is also shown on the far right in Fig. 26. The nose and upper tower components have equal but opposite values of A_Y between the baseline and predefined-cone grids. However, that trend is not necessarily the case for the components downstream of the upper tower.

Figure 27 presents the coefficient convergence history for C_A , C_N , and C_m for the baseline grid and the finer predefined-cone grid at $\alpha = 0^\circ$. The baseline grid has a large oscillation in the coefficient history but the average of the coefficient over several oscillations is level and thus the solution would be considered converged. By using the finer predefined-cone grid on the upper tower and thus a finer resolution for the ACM plumes, this coefficient oscillation is significantly reduced. Both grids give similar predictions for the averaged coefficients.

USM3D predicted asymmetric flow for combinations of powered ACM/AM conditions on a near symmetric configuration supporting asymmetric predictions by OVERFLOW. These results were used to adjust the aerodynamic uncertainties for powered LAV configurations.

VIII. Concluding Remarks

The NASA Constellation program has relied heavily on Computational Fluid Dynamics (CFD) simulations for generating aerodynamic databases and design loads. The NASA Tetrahedral Unstructured Software System (TetrUSS) tool set has served in a supporting role within the Constellation program by investigating various aerodynamic sensitivities and supplementing the aero database for the Orion CEV Aerosciences Project (CAP).

The fast-paced environment of the program has driven the development of largely automated process for generating USM3D solutions. The flow solution process is split into 3 stages: the USM3D input stage, the grid generation stage, and the convergence stage. The USM3D input strategy evolved from several guideline studies and extensive applications. The definition of jet boundary conditions for the Abort Motor and Attitude Control Motor nozzles were derived by an isentropic extrapolation of nozzle exit conditions, provided by CAP, to a plane with the nozzle slight downstream of its throat. Grid generation evolved from relatively simple uniform grids to complex grids with cell clustering driven by flow structures in the USM3D solutions. The solution adaptive gridding was accomplished by combining the use of the TetrUSS GridTool code with the CraftTech CRISP CFD[®] grid adaption code. Solution convergence was largely based on the history of the aerodynamic coefficients. Quantitative characteristics of the evolving behavior for these coefficients as the flow solution develops provided a numerical approach to determining convergence. The adaptive gridding and solution convergence evaluation were automated by using scripts. Post-processing of the USM3D solution was also automated and provided the user various plots to aid in determining the solution's viability.

The TetrUSS system has provided over 2000 solutions on multiple variations of the Crew Module (CM) and the Launch Abort Vehicle (LAV) configurations in thirteen different tasks. Four sample applications illustrate the range of calculations provided by the TetrUSS system on these types of geometries. Guideline studies, such as that on the Apollo CM, provided direction on USM3D input and suitability of various grid approaches. By computing large data sets, such as that on the IDAT CM, USM3D provided corroborating data to be used in defining the aero database. Through comparisons with wind tunnel data such as those conducted using the 19-AA LAV wind tunnel model, USM3D provided not only sting interference corrections but also insight to the effects of sting interference. USM3D computations utilizing the automated grid generation process, such as those conducted on the IDAT CM configuration and the powered 606F LAV configuration, provide the ability to investigate sensitive flow features by variations in grid. The Orion aero-database used the USM3D data to build the aerodynamic uncertainties for both the CM and LAV configurations.

Appendix – Method for Prescribing Jet Boundary Conditions

The methodology for defining the LAV jet boundary conditions in ideal-gas flow solvers presented below was provided via Excel spreadsheet by Mr. James Greathouse at NASA Johnson Spaceflight Center. The jet conditions are provided for by wind tunnel flow conditions or flight LAV trajectory data. A general assumption of one-dimensional isentropic flow is applied to determine the flow conditions at the nozzle exit plane, and then transfer them to the BC plane located just downstream of the jet throat. Figure A1 shows a schematic with the exit plane and BC plane identified.

When using flight trajectory data, the plenum chamber has a non-air gas and thus non-air gas properties. Thus a γ correction needs to be applied after the exit-plane conditions have been determined for the non-air jet gas. After the γ correction, an “imaginary throat for the air nozzle” is determined using the corrected exit plane flow and the known exit plane area ratio. The exit plane conditions corrected for air can now be transferred to the BC plane.

The complete jet BC calculations with a γ correction are given here. For completeness, the relations for one-dimensional isentropic flow through a nozzle are given here:

$$\frac{A}{A^*} = \frac{1}{M} \left[\frac{2}{\gamma+1} \left(1 + \frac{\gamma-1}{2} M^2 \right) \right]^{\frac{\gamma+1}{2(\gamma-1)}} \quad (A1)$$

$$\frac{T_{\text{tot}}}{T} = \left(1 + \frac{\gamma-1}{2} M^2 \right) \quad (A2)$$

$$\frac{p_{\text{tot}}}{p} = \left(1 + \frac{\gamma-1}{2} M^2 \right)^{\frac{\gamma}{\gamma-1}} \quad (A3)$$

$$\frac{\rho_{\text{tot}}}{\rho} = \left(1 + \frac{\gamma-1}{2} M^2 \right)^{\frac{1}{\gamma-1}} \quad (A4)$$

1. Prescribe initial conditions and parameters.

a. Freestream conditions:

$$M_\infty, p_\infty, T_\infty, \rho_\infty, q_\infty, S_{\text{ref}}, \text{ and } a_\infty = (\gamma_{\text{air}} p_\infty / \rho_\infty)^{1/2}$$

$$\gamma_{\text{air}} = 1.4, MW_{\text{air}} = 28.996, R_{\text{air}} = R_{\text{universal}} / MW_{\text{air}} = 1716.47$$

b. Jet plenum gas properties (for hot jet calculations):

$$\text{For hot-jet conditions: } \gamma_{\text{jet}} = 1.25, MW_{\text{jet}} = 26.922, R_{\text{jet}} = R_{\text{universal}} / MW_{\text{jet}} = 1846.78, T_{\text{tot,jet}}$$

$$\text{For wind tunnel conditions: } \gamma_{\text{jet}} = 1.4, MW_{\text{jet}} = 28.996, R_{\text{jet}} = R_{\text{universal}} / MW_{\text{air}} = 1716.47, T_{\text{tot,jet}}$$

c. Geometric areas for nozzle exit, throat, and BC plane:

$$A_e, A_t, \text{ and } A_{\text{BC}}$$

d. Assume $A^* = A_t$ and compute choked nozzle area ratio for the non-air jet flow:

$$A_e / A^* = A_e / A_t$$

2. Expand plenum chamber conditions to nozzle exit plane using jet gas properties.

a. Using γ_{jet} , adjust nozzle exit Mach number, $M_{e,\text{jet}}$, in Eqn. A1 to match the choked area ratio with the geometric area ratio:

$$(A_e / A^*)_{\text{jet}} = A_e / A_t$$

$$\Rightarrow \text{This defines } M_{e,\text{jet}}.$$

b. Substitute γ_{jet} and $M_{e,\text{jet}}$ into Eqns. A2-A4 to compute isentropic relations at nozzle exit:

$$(p_{\text{tot}} / p_e)_{\text{jet}} \quad (T_{\text{tot}} / T_e)_{\text{jet}} \quad (\rho_{\text{tot}} / \rho_e)_{\text{jet}}$$

3. Calculate nozzle exit plane conditions assuming jet gas properties.

- a. Define a target nozzle thrust coefficient:

$$CT_{\text{target}} = (\text{target thrust}) / (q_{\infty} S_{\text{ref}})$$

- b. Adjust plenum chamber pressure, p_{tot} in thrust equation:

$$CT = \left[p_{\text{tot}} / \left((p_{\text{tot}} / p_e)_{\text{jet}} \right) \cdot A_e \left(1 + \gamma_{\text{jet}} M_{e,\text{jet}}^2 \right) \cdot \cos(25^\circ) \right] / (q_{\infty} S_{\text{ref}})$$

until CT matches CT_{target} . The “ $\cos(25^\circ)$ ” term sets the CT in the body axial direction.

\Rightarrow This determines p_{tot} .

- c. Calculate the total density, ρ_{tot} , using the gas equation:

$$\rho_{\text{tot}} = p_{\text{tot}} / (R_{\text{jet}} T_{\text{tot}})$$

note: T_{tot} defined in Step 1(b)

- d. Complete the nozzle exit conditions from known quantities;

$$p_{e,\text{jet}} = p_{\text{tot}} / (p_{\text{tot}} / p_e)_{\text{jet}}$$

$$T_{e,\text{jet}} = T_{\text{tot}} / (T_{\text{tot}} / T_e)_{\text{jet}}$$

$$\rho_{e,\text{jet}} = p_{e,\text{jet}} / (R_{\text{jet}} T_{e,\text{jet}})$$

$$V_{e,\text{jet}} = M_{e,\text{jet}} (\gamma_{\text{jet}} R_{\text{jet}} T_{e,\text{jet}})^{1/2}$$

4. Switch from jet gas to air and recalculate the chamber conditions. The general assumption is to maintain the thrust. Since thrust is a function of exit-plane pressure and jet momentum, the values of nozzle exit pressure, density, and velocity will remain unchanged. The primary impact of switching gas from jet gas to air is a change in the nozzle exit temperature. This directly impacts the speed of sound and exit Mach number, which in turn alters the values of the isentropic relations in Eqns. A2-A4 and the total conditions.

- a. Adjust nozzle exit jet temperature and Mach number for air:

$$T_{e,\text{air}} = p_{e,\text{jet}} / (R_{\text{air}} \rho_{e,\text{jet}})$$

$$M_{e,\text{air}} = V_{e,\text{jet}} / (\gamma_{\text{air}} R_{\text{air}} T_{e,\text{air}})^{1/2}$$

- b. Assign remaining jet properties to nozzle exit as air:

$$\rho_{e,\text{air}} = \rho_{e,\text{jet}}$$

$$p_{e,\text{air}} = p_{e,\text{jet}}$$

$$V_{e,\text{air}} = V_{e,\text{jet}}$$

- c. Perform sanity check of thrust by comparing new CT_{air} with CT_{target} :

$$CT_{\text{air}} = \left[p_{e,\text{air}} \cdot A_e \left(1 + \gamma_{\text{air}} M_{e,\text{air}}^2 \right) \cdot \cos(25^\circ) \right] / (q_{\infty} S_{\text{ref}})$$

- d. Compute new isentropic relations at nozzle exit using Eqns. A2-A4 with γ_{air} and $M_{e,\text{air}}$:

$$(p_{\text{tot}} / p_e)_{\text{air}} \quad (T_{\text{tot}} / T_e)_{\text{air}} \quad (\rho_{\text{tot}} / \rho_e)_{\text{air}}$$

- e. Compute for total jet conditions with assumed air:

$$p_{\text{tot},\text{air}} = p_{e,\text{air}} (p_{\text{tot}} / p_e)_{\text{air}}$$

$$T_{\text{tot},\text{air}} = T_{e,\text{air}} (T_{\text{tot}} / T_e)_{\text{air}}$$

$$\rho_{\text{tot},\text{air}} = \rho_{e,\text{air}} / (\rho_{\text{tot}} / \rho_e)_{\text{air}}$$

5. Calculate an “imaginary throat for the air nozzle”, and then A/A^* at the BC plane just down stream of the throat.

- a. Use Eqn. A1 to compute new $(A_e/A^*)_{\text{air}}$ using γ_{air} and $M_{e,\text{air}}$.

- b. Compute new choked throat area A^* .

- c. Calculate A_{BC}/A_{air}^*

$$A_{air}^* = A_e / (A_e / A_{air}^*)$$

- d. Calculate the new choked nozzle area ratio, A_{BC}/A_{air}^* .

6. Propagate the exit plane conditions to the BC plane.

- a. Using γ_{air} , adjust Mach number on the BC plane, $M_{BC,air}$, in Eqn. A1 to match the new choked area ratio with the geometric area ratio (A_{BC} / A_{air}^*).

\Rightarrow This defines $M_{BC,air}$.

- b. Substitute γ_{air} and $M_{BC,air}$ into isentropic relations Eqns. A2-A4 to compute BC-plane ratios:

$$(p_{tot} / p_{BC})_{air} \quad (T_{tot} / T_{BC})_{air} \quad (\rho_{tot} / \rho_{BC})_{air}$$

- c. Compute the BC-plane properties:

$$p_{BC} = p_{tot,air} / (p_{tot} / p_{BC})_{air}$$

$$T_{BC} = T_{tot,air} / (T_{tot} / T_{BC})_{air}$$

$$\rho_{BC} = \rho_{tot,air} (\rho_{tot} / \rho_{BC})_{air}$$

$$V_{BC} = M_{BC} (\gamma_{air} R_{air} T_{BC})^{1/2}$$

- d. Compute USM3D non-dimensional BC values using freestream conditions:

$$\rho_{USM3D} = \rho_{BC} / \rho_{\infty}$$

$$V_{USM3D} = V_{BC} / a_{\infty}$$

$$p_{USM3D} = p_{BC} / (\gamma_{air} p_{\infty})$$

7. Apply jet boundary conditions.

- a. Directly apply ρ_{USM3D} and p_{USM3D} across BC plane
- b. Smoothly fan the velocity vectors from the center of the BC plane until parallel to the nozzle walls. Maintain nozzle axis component of V_{USM3D} constant across plane.

References

- ¹Frink, N. T., Pirzadeh, S. Z., Parikh, P. C., Pandya, M. J. (2000), "The NASA Tetrahedral Unstructured Software System", *Aeronautical Journal*, Vol. 104, No. 1040 (491-499). TetrUSS website: <http://tetruss.larc.nasa.gov>.
- ²Pandya, M.J., Frink, N.T., Abdol-Hamid, K.S., Samareh, J.A., Parlette, E.B., and Taft, J.R., "Enhancements to TetrUSS for NASA Constellation Program," AIAA 2011-1111, January 2011.
- ³Pirzadeh, S. Z., "Three-Dimensional Unstructured Viscous Grids by the Advancing Layers Method," *AIAA Journal*, Vol. 33, No. 1, 1996, pp. 43-49.
- ⁴Pirzadeh, S. Z., "Advanced Unstructured Grid Generation for Complex Aerodynamic Applications," *AIAA Journal*, Vol. 48, No. 5, 2010, pp. 904-915.
- ⁵Samareh, J., "GridTool: A Surface Modeling and Grid Generation Tool," Proceedings of the Workshop on Surface Modeling, Grid Generation, and Related Issues in CFD Solutions, NASA CP-3291, 9-11 May, 1995.
- ⁶Cavallo, P., Grismer, M., "A Parallel Adaptation Package For Three-Dimensional Mixed-Element Unstructured Meshes", *Journal of Aerospace Computing, Information, and Communication* 2005, 1542-9423 Vol. 2, No. 11, (433-451) doi: 10.2514/1.16220.
- ⁷Frink, N. T., "Upwind scheme for solving the Euler equations on unstructured tetrahedral meshes," *AIAA Journal*, Vol. 30, No. 1, 1992, pp. 70-77.
- ⁸Frink, N. T., "Tetrahedral unstructured Navier-Stokes method for turbulent flows," *AIAA Journal*, Vol. 36, No. 11, 1998, pp. 1975-1982.
- ⁹"CRISP CFD User's Manual, Version 1.5," Combustion Research and Flow Technology, Inc., 6210 Keller's Church Road, Pipersville, PA 18947, February 2007.
- ¹⁰McMillin, S. N., Frink, N. T., "USM3D Flight-to-WTT Reynolds Number Scaling for 60-AA ALAS Including Abort Motor Jets," NASA Langley Research Center, Rept. EG-CAP-11-55, Hampton, VA, April 2011.
- ¹¹Frink, N. T., McMillin, S. N., "CEV/CM CFD Simulation Guidelines for USM3D Navier-Stokes Solver," NASA Langley Research Center, Rept. EG-CAP-06-34, Hampton, VA, October 2006.
- ¹²McMillin, S. N., Frink, N. T., "ACM USM3D analysis for the -068 LAV in both 59-AA and Free-flight Configurations," NASA Langley Research Center, Rept. EG-CAP-09-158, Hampton, VA, October 2009.
- ¹³Brauckmann, G. J., Greathouse, J. S., and White, M. E., "Rocket Plume Scaling for Orion Wind Tunnel Testing," 29th AIAA Applied Aerodynamics Conference, Honolulu, HI, 27-30 June 2011, American Institute of Aeronautics and Astronautics, Reston, VA (submitted for publication).
- ¹⁴Robinson, P.R., et. al., "Orion Aerodynamic Databook," NASA CXP-72167, 2006-2010.
- ¹⁵Childs, R. E., Garcia, J. A., Melton, J. A., Rogers, S. E., Shestopalov, A. J., and Vicker, D. J., "Overflow Simulation Guidelines for Orion Launch Abort Vehicle Aerodynamic Analyses," 29th AIAA Applied Aerodynamics Conference, Honolulu, HI, 27-30 June 2011, American Institute of Aeronautics and Astronautics, Reston, VA (submitted for publication).
- ¹⁶McMillin, S. N., Frink, N. T., "Assessment of Data Issues from LAV 19-AA Wind Tunnel Test Using TetrUSS", NASA Langley Research Center, Rept. EG-CAP-07-85, Hampton, VA, June 2007.

Table 1. List of USM3D studies.

Task ID	Geometry	Title/Objective
Guideline 1	Apollo CM	CEV/CM CFD Simulation Guidelines for USM3D Navier-Stokes Solver
		Develop simulation guidelines for computations on the CEV CM
AR-10	CEV CM	USM3D Solutions for CEV CM Database
		Generate data for the CEV CM aerodynamic database
Guideline 2	Apollo LAS	Unpowered LAS Simulation Guidelines for USM3D Navier-Stokes Solver
		Develop simulation guidelines for computations on the unpowered LAV
AR-26	604-Mod6 LAV	Assessment of 604-Mod6 LAV w/o Canards or Plume Effect Using USM3D
		Generate data for an assessment database of the 604-Mod6 LAV
AR-41	19-AA LAV	USM3D Analysis of the 19-AA LAV WTT
		Generate data to assess the sting influence on the 19-AA wind tunnel data
AR-60	605-054 LAV	USM3D Reynolds Number Sensitivity Analysis Using the 19-AA LAV
		Generate data to assess Reynolds number effects on the LAV aerodynamics
AR-76	606-068 LAV	ACM USM3D Analysis for the 606-068 LAV in Both 59-AA and Free-flight Configurations
		Generate data for the 59-AA LAV wind tunnel model geometry at both wind tunnel and flight Reynolds number conditions with the ACMs firing
Guideline 3	ALAS11r3b	LAV with AM Jets On Simulation Guidelines for USM3D Navier-Stokes Solver
		Develop simulation guidelines for computations on LAV with AMs firing
AR-100	ALAS11r3b	USM3D Flight-to-WTT Reynolds Number Scaling for 60-AA ALAS Including Abort Motor Jets
		Generate data for the 60-AA LAV wind tunnel model at both wind tunnel and flight Reynolds number conditions with the AMs firing
AR-105	606F LAV	USM3D Analysis of AM Thrust Offset
		Generate data to evaluate the jet effects of the AM plume on the 606F LAV as a function of thrust offset
AR-112	606F LAV	USM3D Analysis of AM+ACM Jet Interaction
		Generate data to evaluate the jet effects of the combination of AM and ACM plumes on the 606F LAV
AR-122	IDAT CM	USM3D IDAT CM Cases for the v0.6 Aero Database
		Generate data for the IDAT CM aerodynamic database version 0.60
AR-128	26-AA LAV	USM3D Analysis of the 26-AA WTT
		Generate data for the 26-AA LAV wind tunnel model at conditions where OVERFLOW did not match wind tunnel test data

Table 2. Information for the USM3D tasks.

Task ID	Geometry	M_∞	α , deg.	β deg.	Re_D $\times 10^6$	TR	CT	Ncell $\times 10^6$	Date
Predefined Wake Grids									
Guideline 1	Apollo CM	0.7 - 1.2	0 - 180	0	8	-	-	6	3/06
AR-10	CEV CM	0.7 - 2.5	0 - 180	0	10 - 18	-	-	6	8/06
Base Grids									
Guideline 2	Apollo LAS	0.5 - 1.2	-20 - 0	0	13 - 48	-	0	20	9/06
AR-26	604-Mod6 LAV					-	0	20	11/06
AR-41	605-054 LAV	0.5	0 - 180	0	3	-	0	14	4/07
AR-60	605-054 LAV	0.5	0, 10	0	3, 48	-	0	14	6/07
Solution Adapted Grids									
AR-76	606-068 LAV	0.3 - 0.7	-5 - 20	0, 10	29 - 67	0 - 0.14	0	27	11/07
Guideline 3	ALAS11r3b	0.7 - 1.2	0 - -8		2.5	-	0, 4	29	1/09
AR-100	ALAS11r3b	0.7 - 2.5	0 - -8	0	2.5 - 80	-	0 - 16	29	5/09
AR-105	606F LAV	0.5 - 3.0	-10 - 10	0	47 - 83	-	0 - 4	45	8/09
AR-112	606F LAV	0.9 - 1.6	-10 - 10	0	47 - 83	0 - 0.1	0 - 4	58	6/10
AR-122	IDAT CM	0.5 - 8	0 - 180	0	2.9 - 22	-	-	25	10/10
AR-128	26-AA LAV	0.5 - 1.3	-15 - 15	0	2.9	-	1.5 - 6	43	4/11

Table 3. Steps of the flow solution process.

Step	Action
USM3D Input Stage	
1	Create input files for USM3D: a. boundary condition input. b. jet inflow boundary condition input. c. flow and geometry input.
Grid Generation Stage	
2	Generate the baseline grid using VGRID40.
3	Optimize baseline grid using the CraftTech CRISP CFD [®] code.
4	Run USM3D on baseline grid for 3,000 iterations in 1 st order and then 10,000 iterations in 2 nd order.
5	Perform grid adaptation using CraftTech CRISP CFD [®] code: a. adapt to gradients of ρ , u , v , w , and p . b. constrain minimum spacing to 1 inch (full scale).
6	Interpolate baseline solution onto adapted grid for a solution restart in USM3D.
Convergence Stage	
7	Restart USM3D on adapted grid and run in 1st order mode for 1,500 iterations.
8	Restart USM3D in 2 nd order mode and do the following: a. simultaneously monitor USM3D output files to check convergence criteria at regular timed intervals. b. stop solution when the first 3 convergence criteria are met to examine solution.
9	User examines the solution and decides from the following: a. extend the solution by repeating Step 8. b. accept the solution and begin post-processing.

Table 4. Convergence Criteria.

Criterion	Definition
1	Variation of C_L , C_D , C_m , C_N , and C_A less than 1% over last 1000 iterations
2	Average of last 1000 iterations within 1% of average of preceding 1000 iterations
3	Maximum delta of coefficients < 0.004 over last 1000 iterations
4	L2-norm solution residual of all flow variables drop at least 2.5-orders of magnitude
5	Maximum delta of the two iteration intervals averages < 0.002

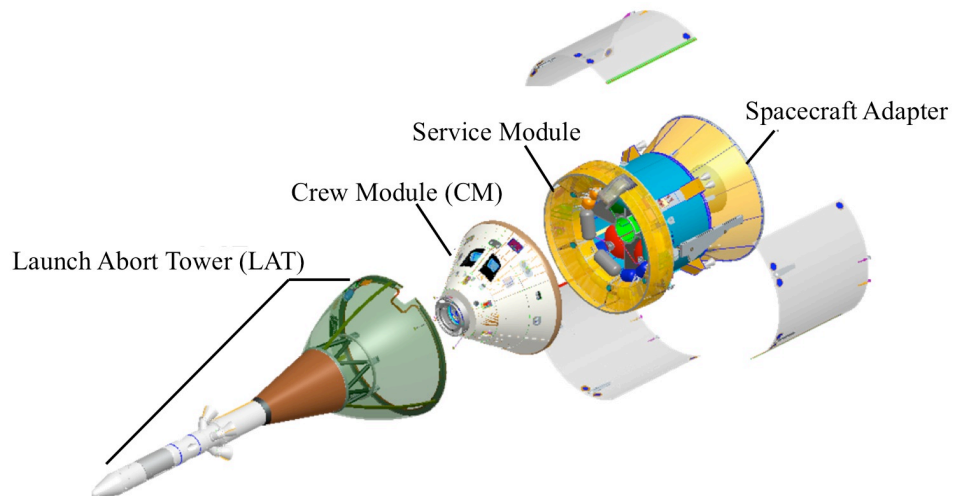
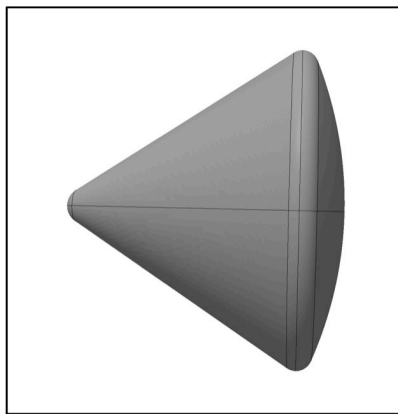
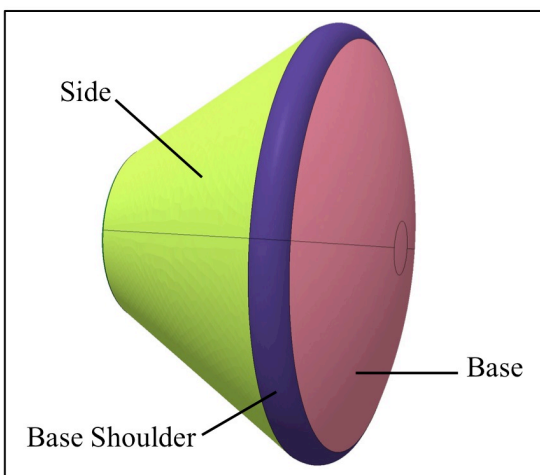


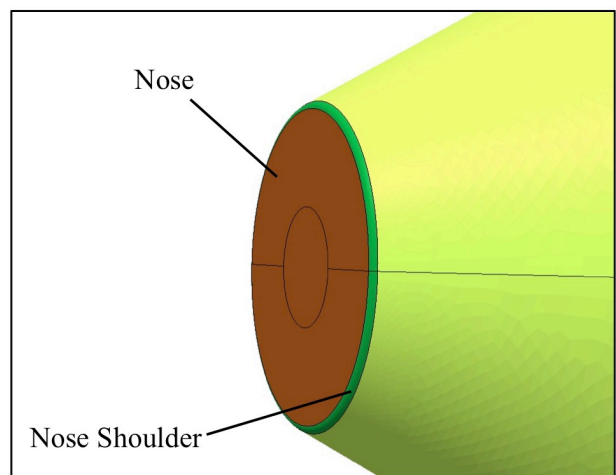
Figure 1. Major components of the Orion CEV.



(a) Side view of the Apollo CM configuration with the apex cover.

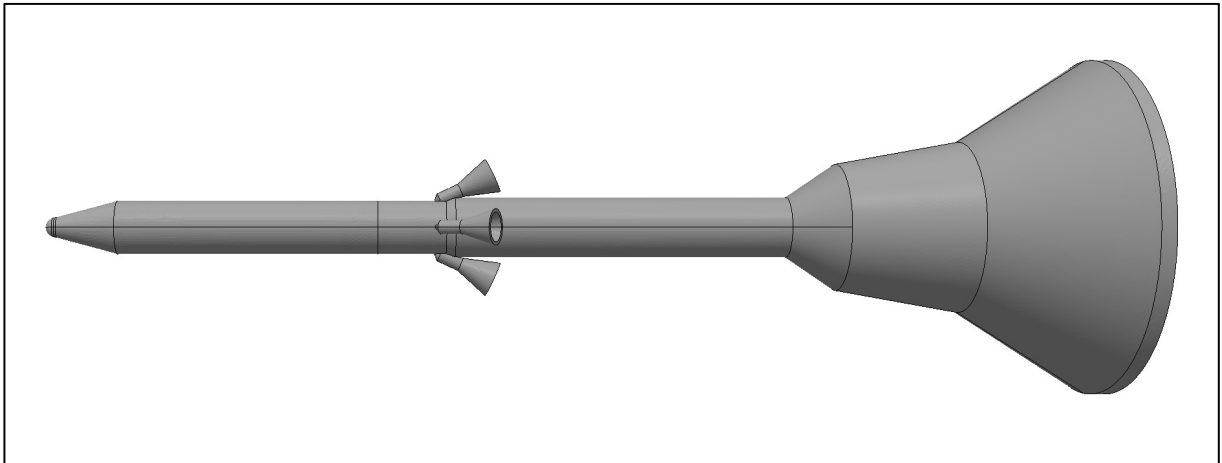


(b) Oblique view of the IDAT CM.

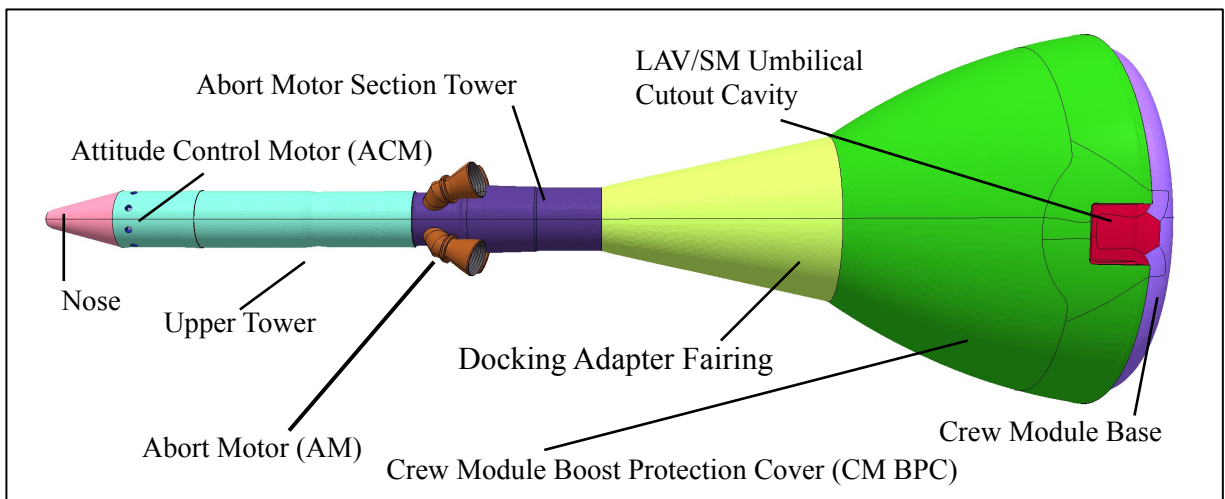


(c) Close-up on the nose of the IDAT CM.

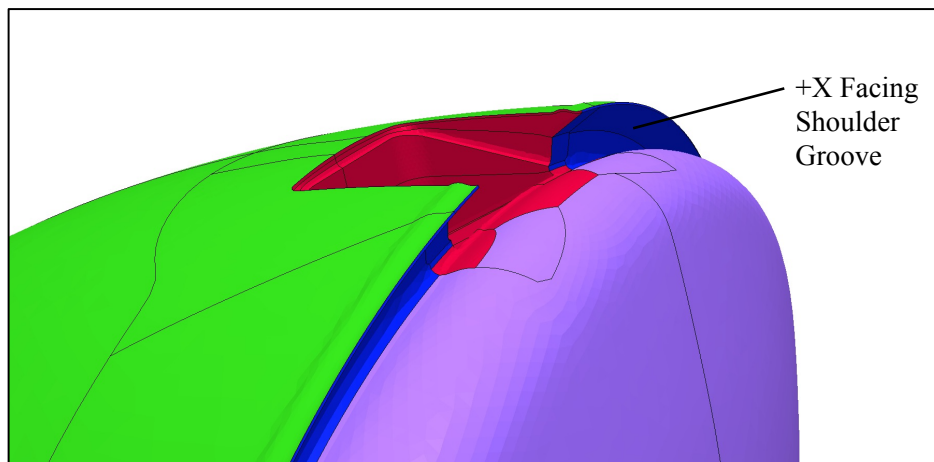
Figure 2. Views of two CM configurations.



(a) Top view of the 605-054 LAV configuration.

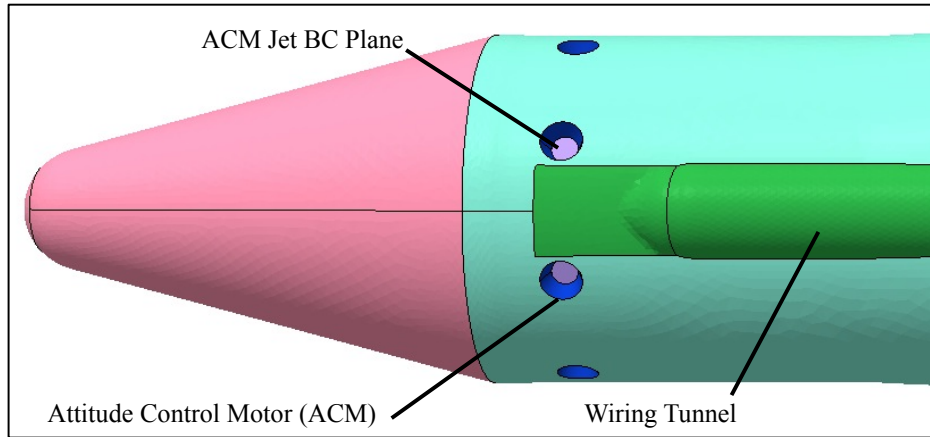


(b) Top view of the 606F LAV configuration.

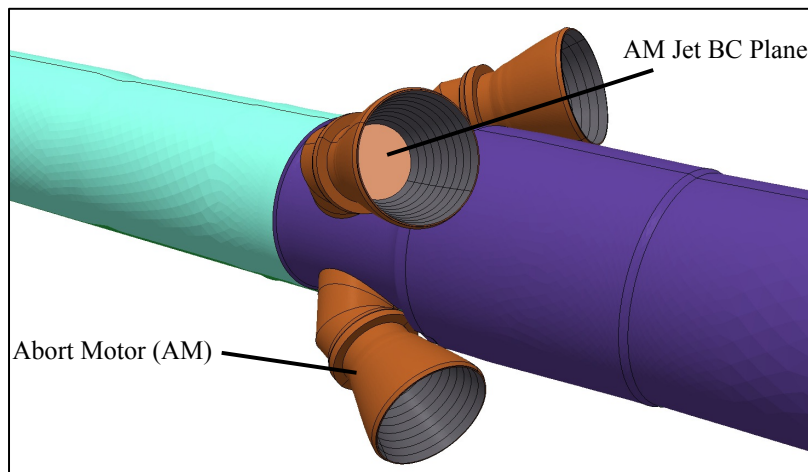


(c) Close-up on the shoulder groove of the 606F LAV configuration.

Figure 3. Views of two LAV configurations.



(d) Bottom view of the upper tower with the ACMs of the 606F LAV configuration.



(e) Close-up view on the AMs of the 606F LAV configuration.
Figure 3. Concluded.

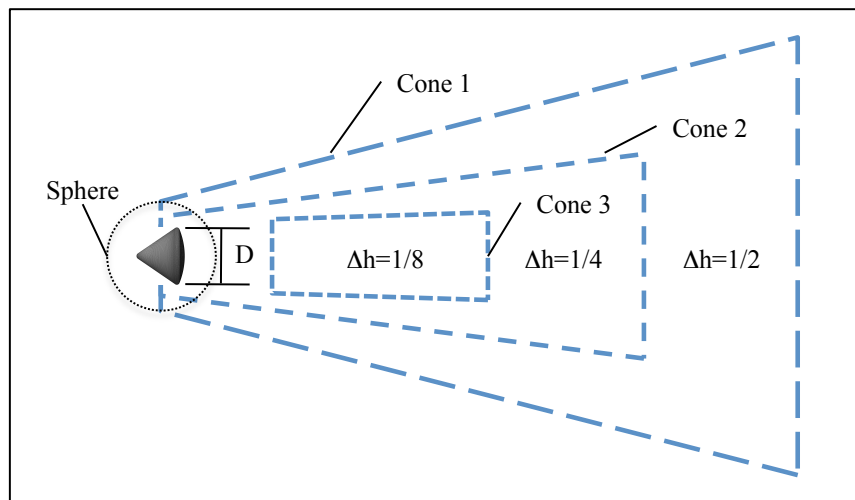
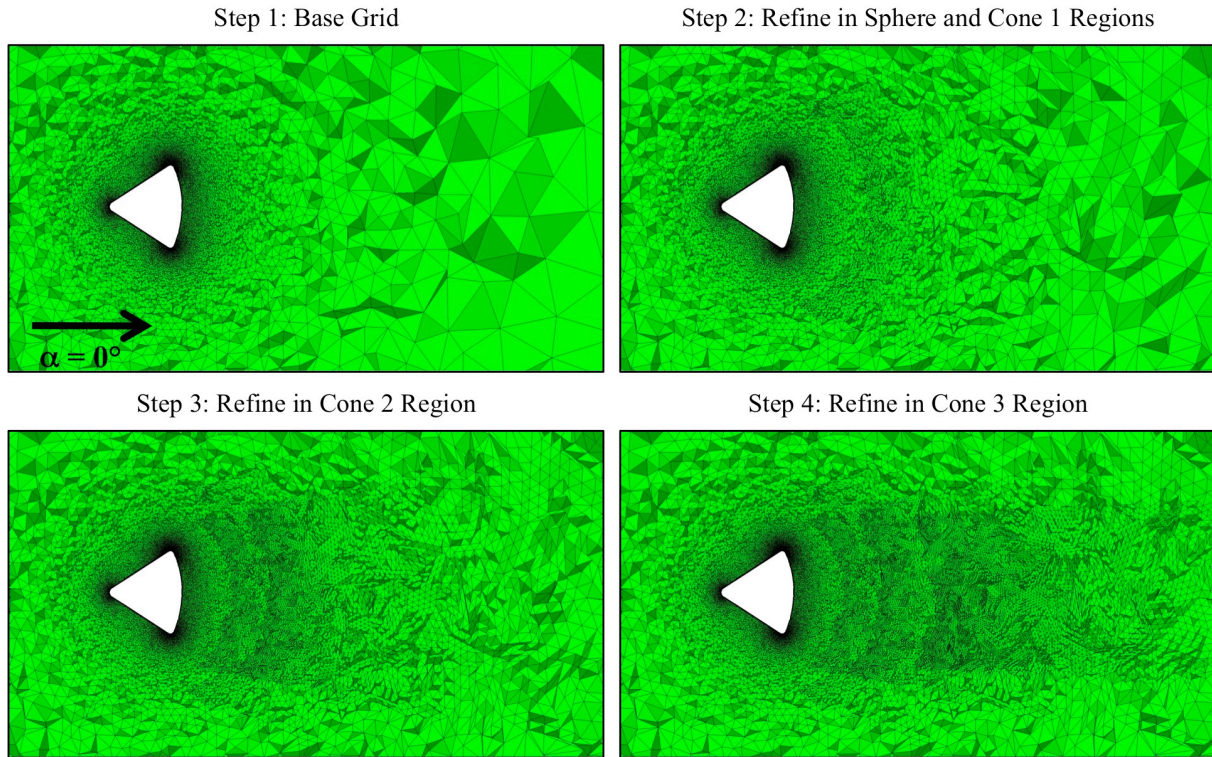
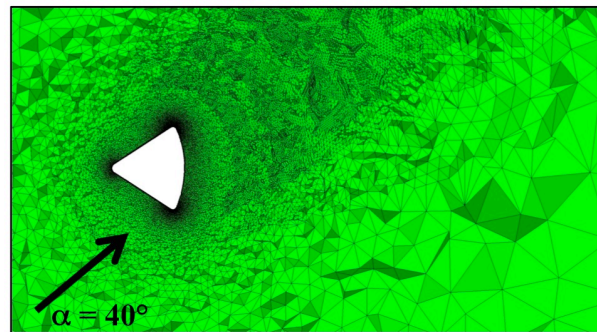


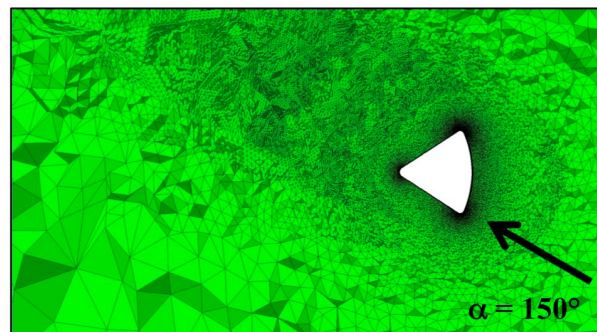
Figure 4. Sketch of predefined wake grid generation using h-refinement method.



(a) Grids at each step of predefined wake grid generation for $\alpha = 0^\circ$.



(b) Predefined wake grid for $\alpha = 40^\circ$.



(c) Predefined wake grid for $\alpha = 150^\circ$.

Figure 5. Grids for the Apollo CM configuration at different angles of attack.

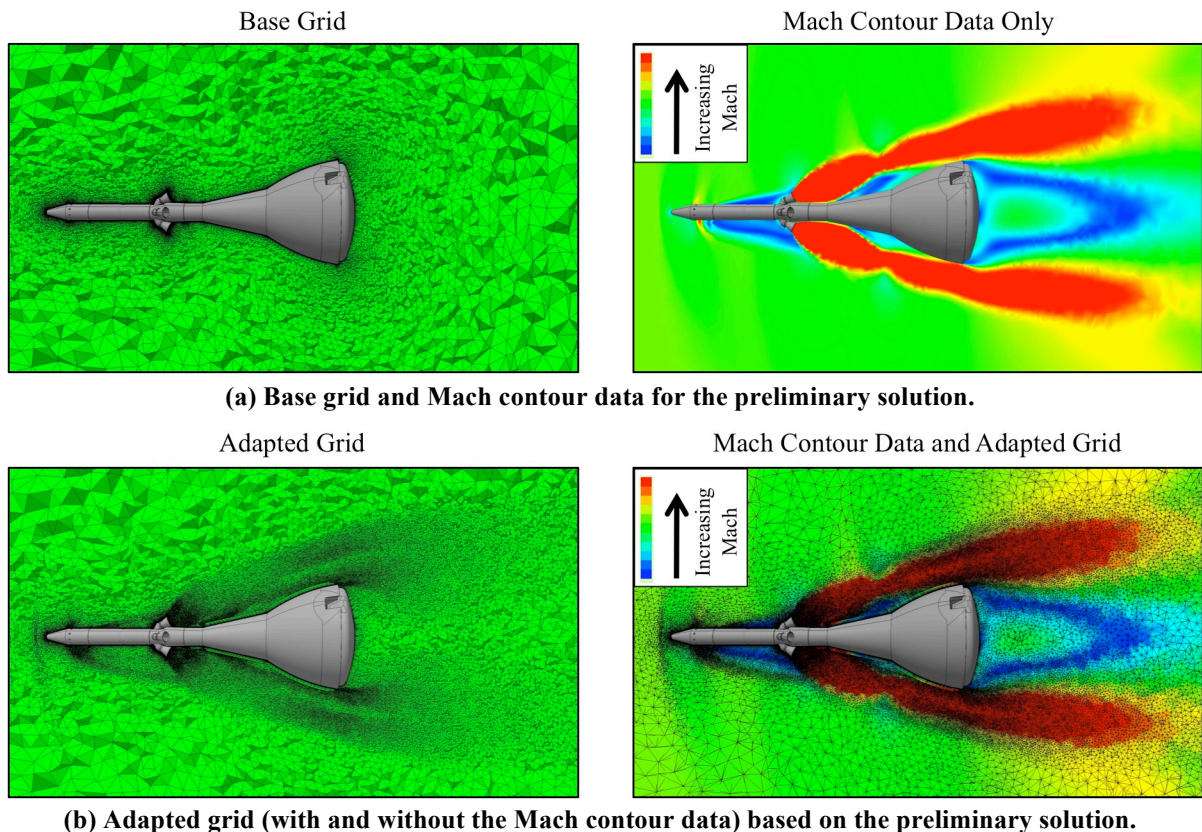


Figure 6. Grid and Mach contour data (on the $\phi = 45^\circ$ plane) from the preliminary solution on the base grid for the 606F LAV configuration at $M_\infty = 1.1$, $\alpha = 5^\circ$, $CT = 4.0$, and $TR = 0.04$.

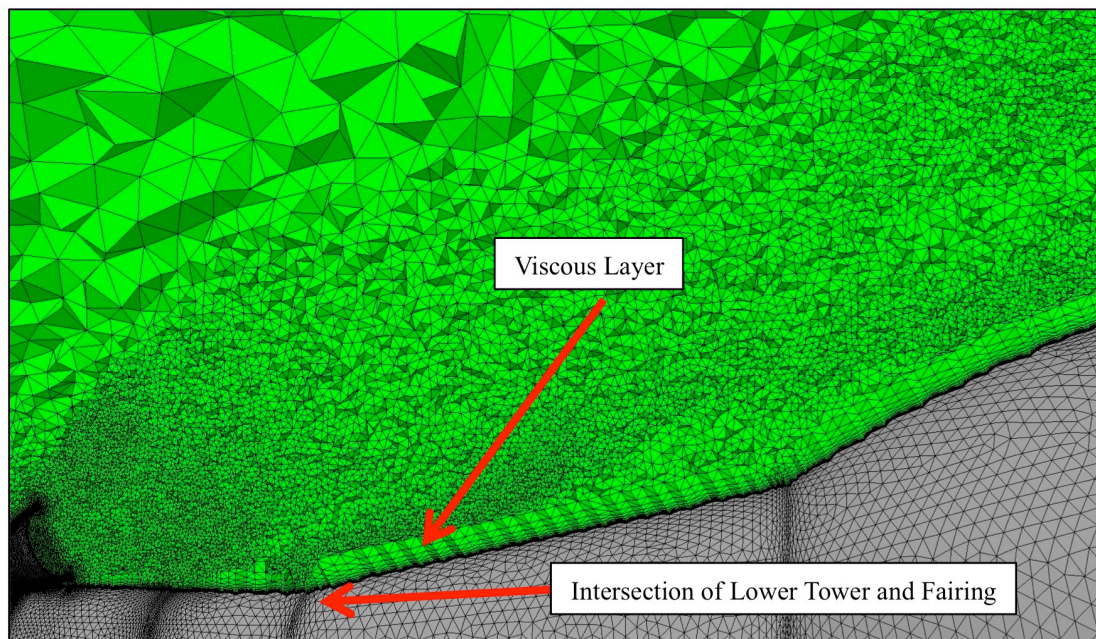


Figure 7. Adapted grid (on the $\phi = 45^\circ$ plane) for the 606F LAV configuration at $M_\infty = 1.1$, $\alpha = 5^\circ$, $CT = 4$, and $TR = 0.04$.

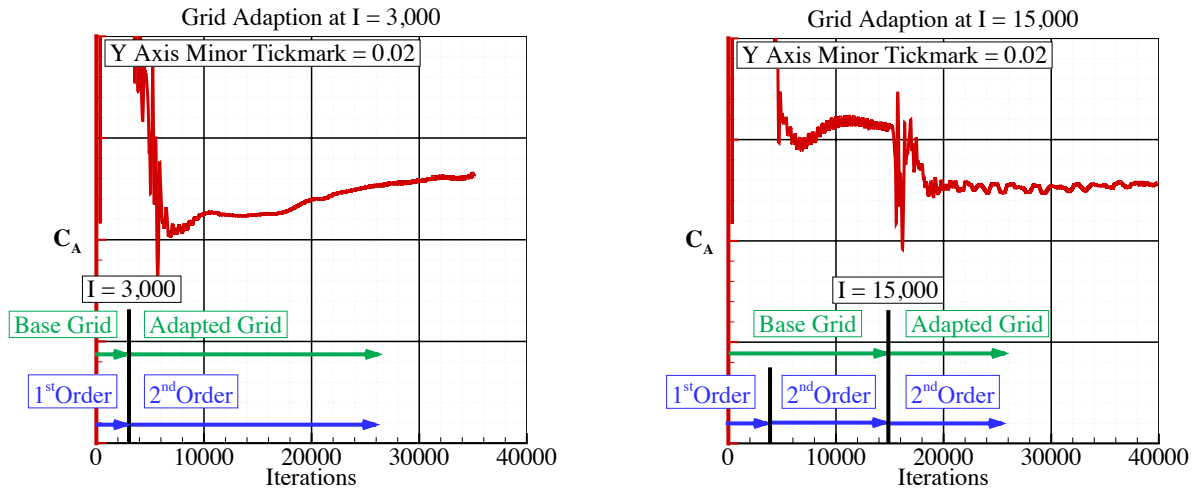
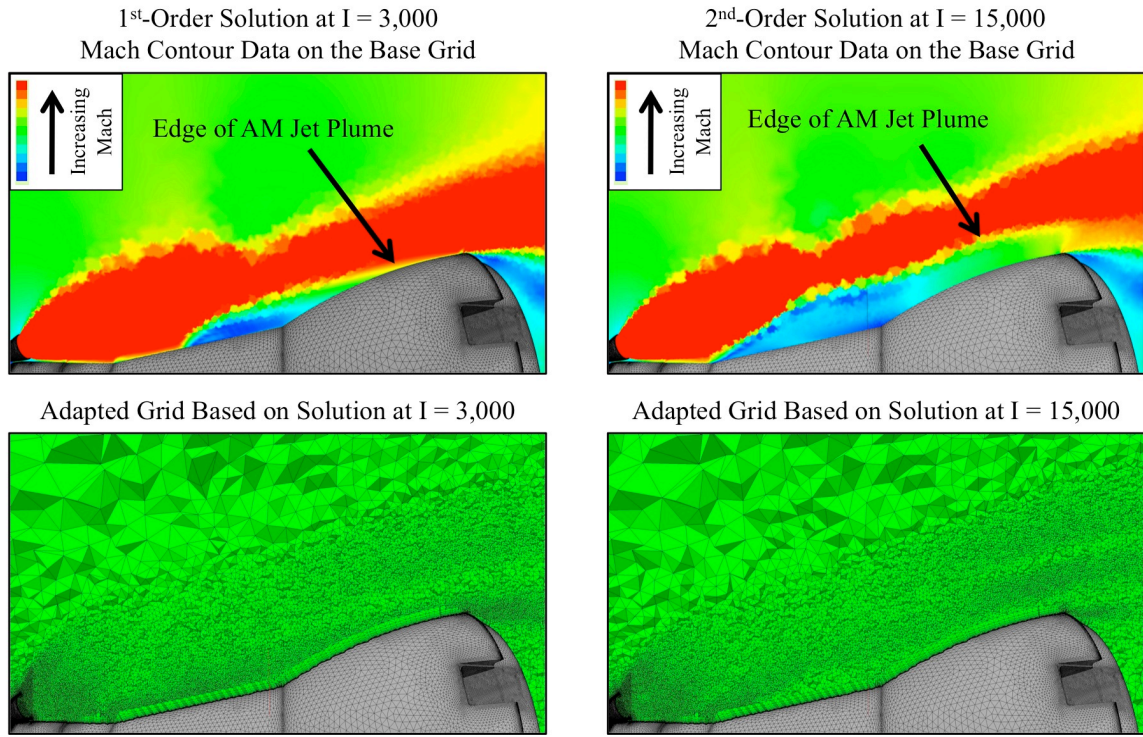
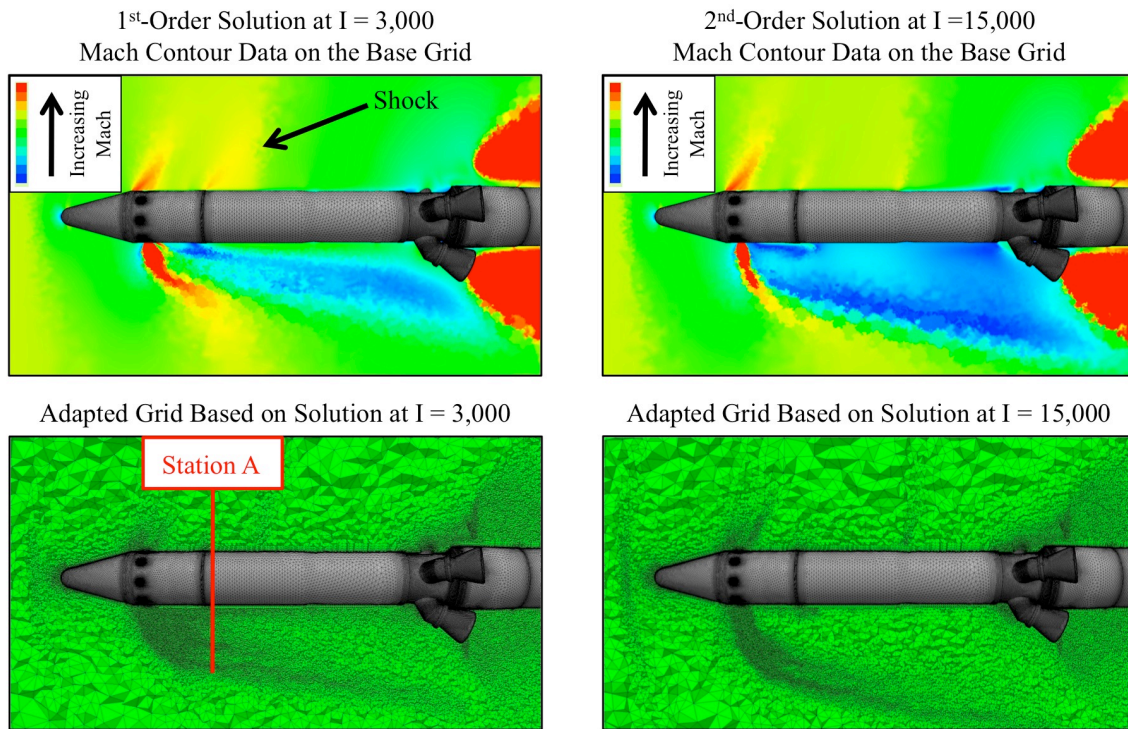


Figure 8. C_A convergence history for two solutions obtained with different adapted grids on the 606F LAV configuration at $M_\infty = 1.1$, $\alpha = 0^\circ$, $CT = 3.0$, and $TR = 0.04$.

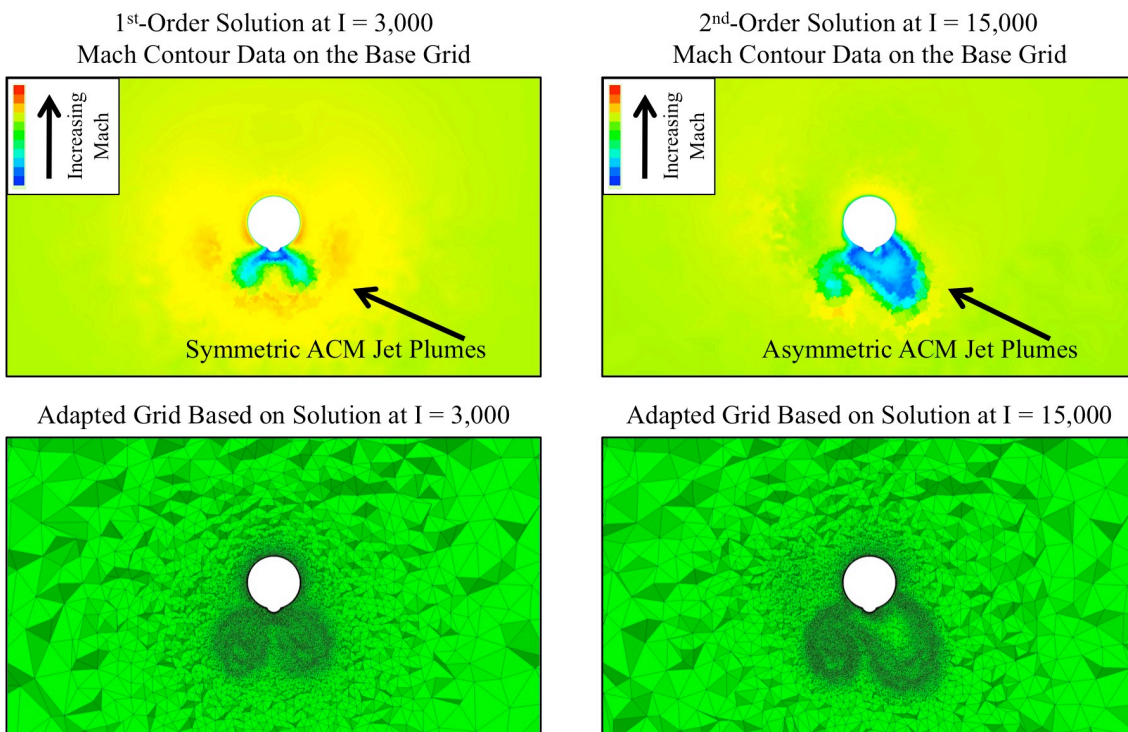


(a) Close-up view on the $\phi = 45^\circ$ plane.

Figure 9. Mach contour data and adapted grids from the 1st-order and 2nd-order solutions for the 606F LAV configuration at $M_\infty = 1.1$, $\alpha = 0^\circ$, $CT = 3.0$, and $TR = 0.04$.



(b) Close-up view on the $\phi = 22.5^\circ$ plane.



(c) Close-up view on the Station A plane.

Figure 9. Concluded.

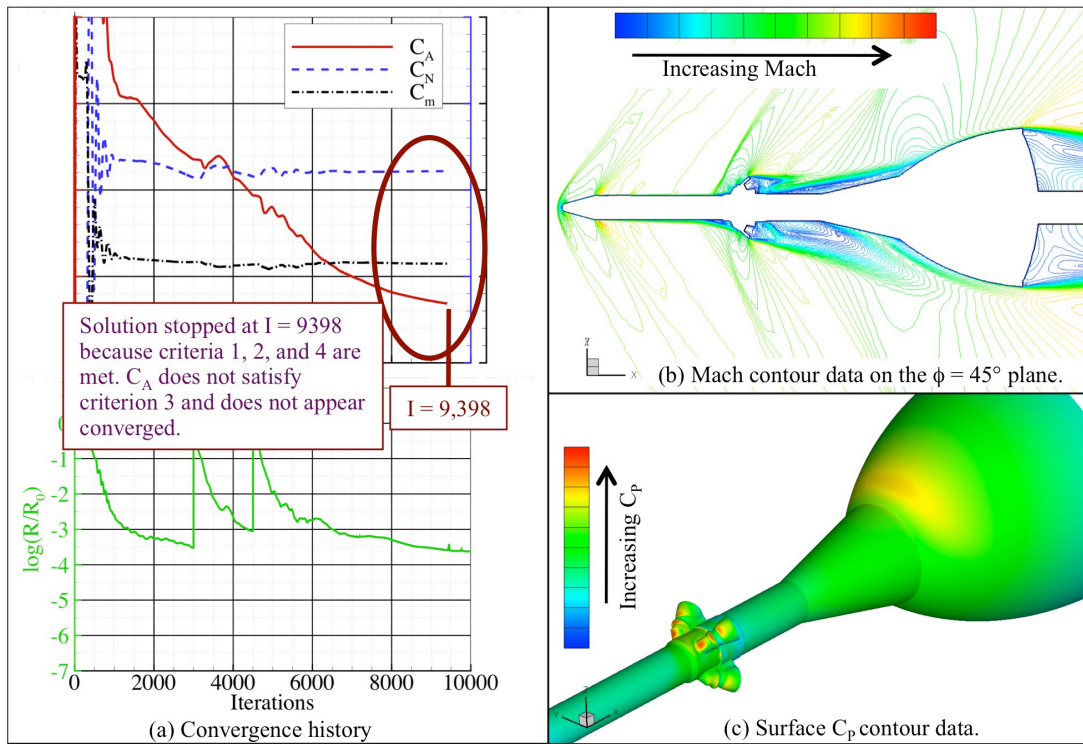


Figure 10. Solution summary chart for the unpowered ALAS11r3b configuration at $M_\infty = 1.3$, $\alpha = -8^\circ$, and $Re_D = 2.5 \times 10^6$ at $I = 9,398$.

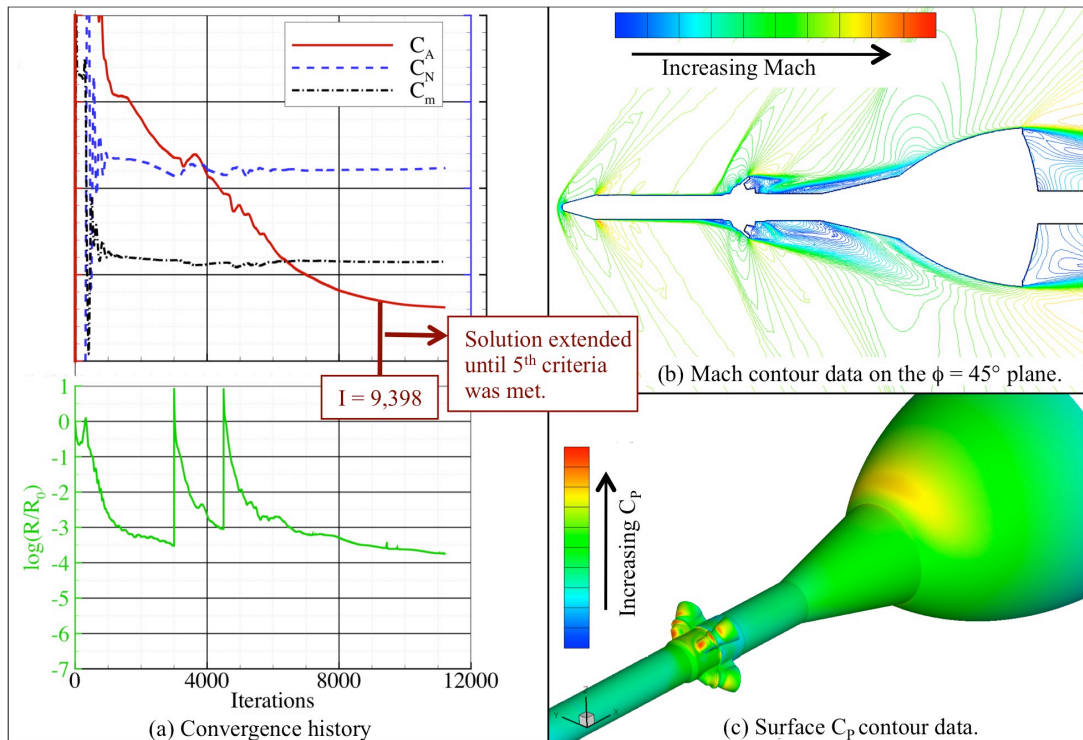
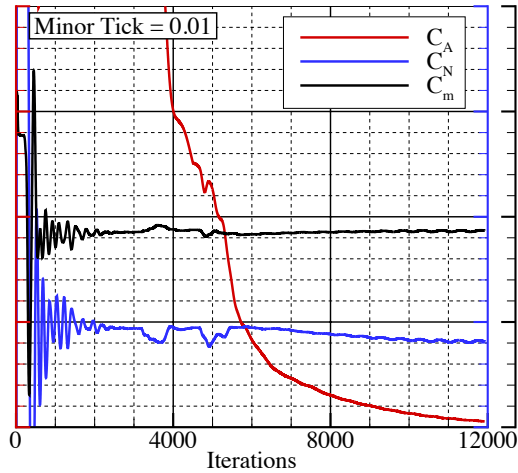
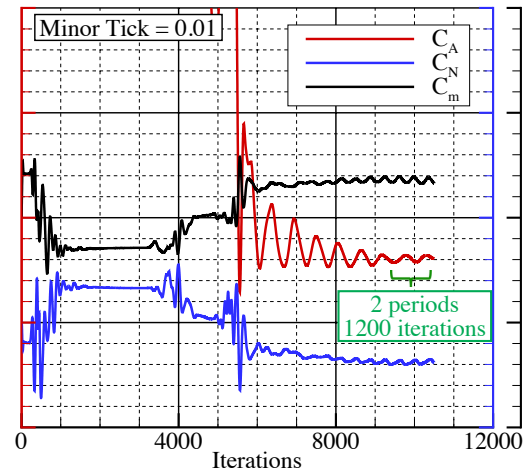


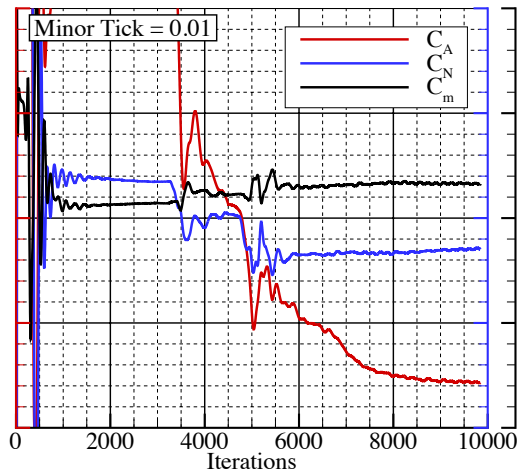
Figure 11. Solution summary chart for the unpowered ALAS11r3b configuration at $M_\infty = 1.3$, $\alpha = -8^\circ$, and $Re_D = 2.5 \times 10^6$ at $I = 11,219$.



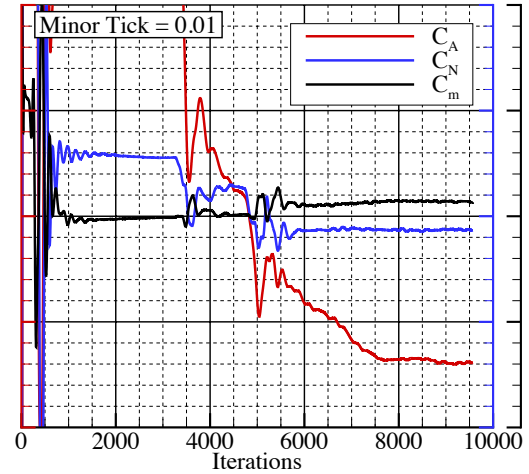
(a) Normal convergence



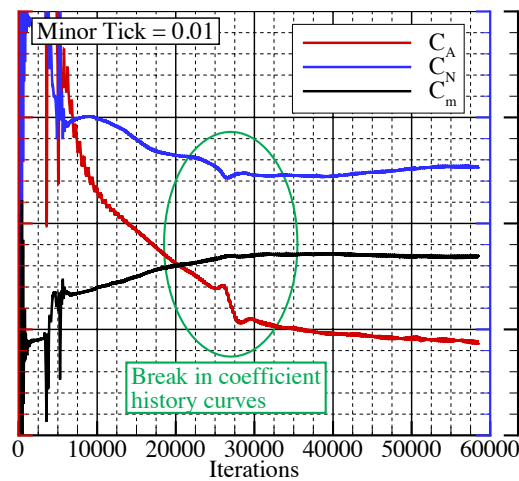
(b) Oscillation convergence



(c) Small oscillation convergence.



(d) Irregular oscillation convergence



(e) Curve break convergence.

Figure 12. Types of coefficient history convergence.

USM3D and Wind Tunnel Data Comparison

	Mach	Rn ($\times 10^6$)	Turbulence Model
○	0.902	9.04	NAA TWT Data
□	0.898	3.30	ARC 11x11 WT Data
●	0.900	8.00	Spalart-Allmaras
■	0.900	8.00	SST
◆	0.900	8.00	k-ε (Linear)
▲	0.900	8.00	k-ε (Non-linear Girimaji)

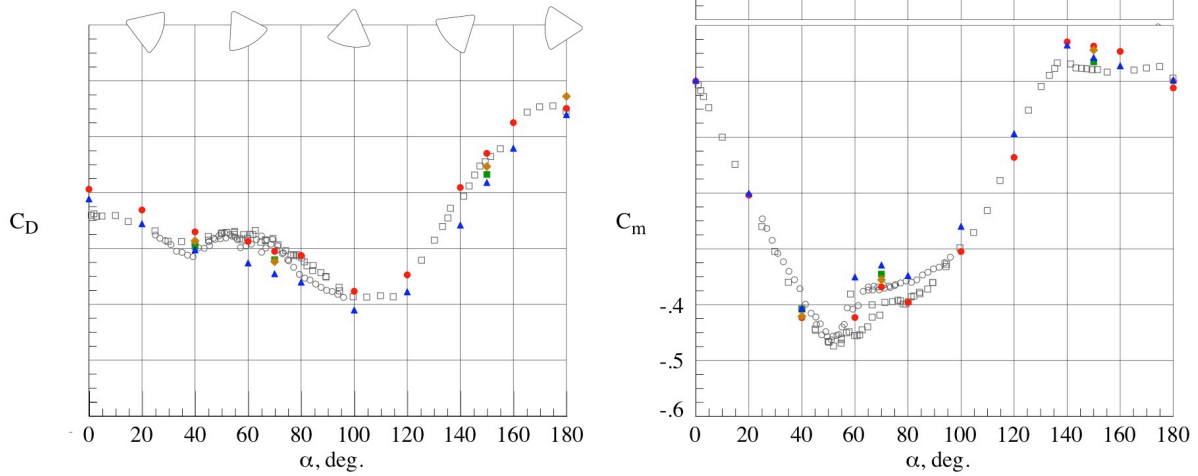


Figure 13. Comparison of USM3D and wind tunnel aerodynamic coefficient data for the Apollo CM configuration at $M_\infty = 0.9$ and $0^\circ \leq \alpha \leq 180^\circ$.

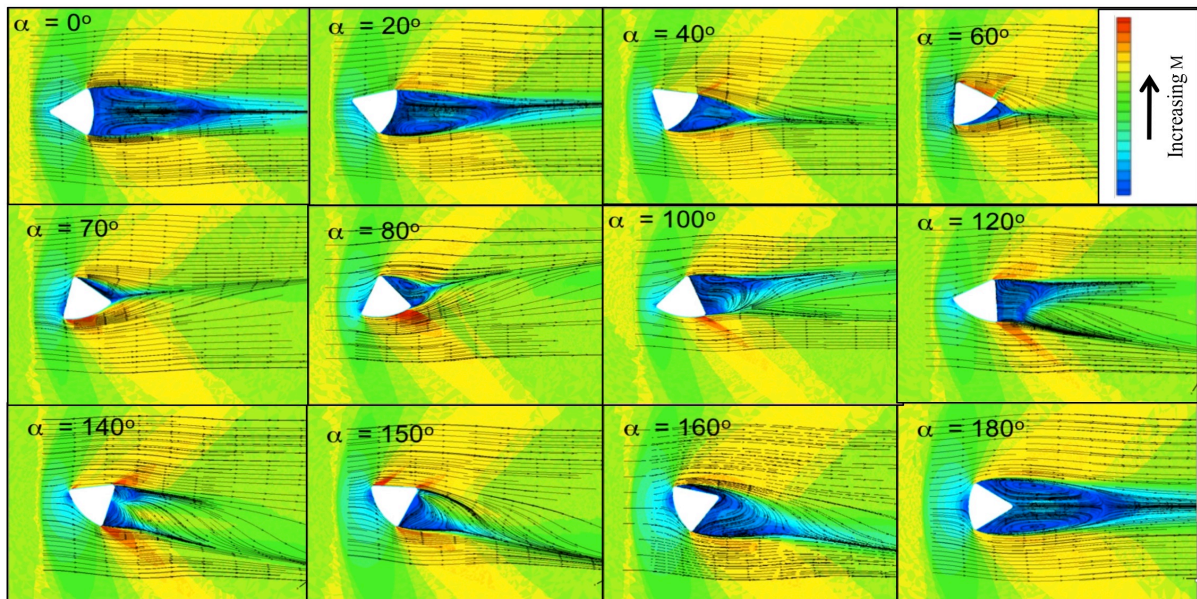


Figure 14. USM3D Mach contour data for the Apollo CM configuration at $M_\infty = 0.9$ and $0^\circ \leq \alpha \leq 180^\circ$.

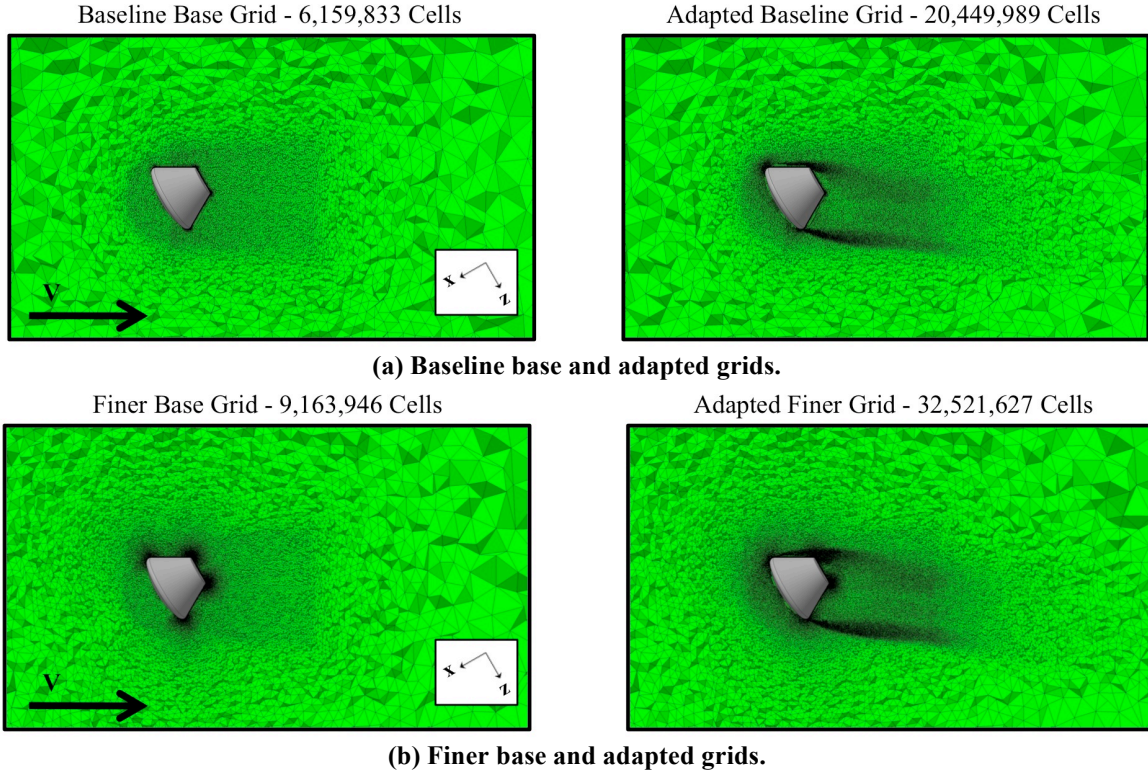
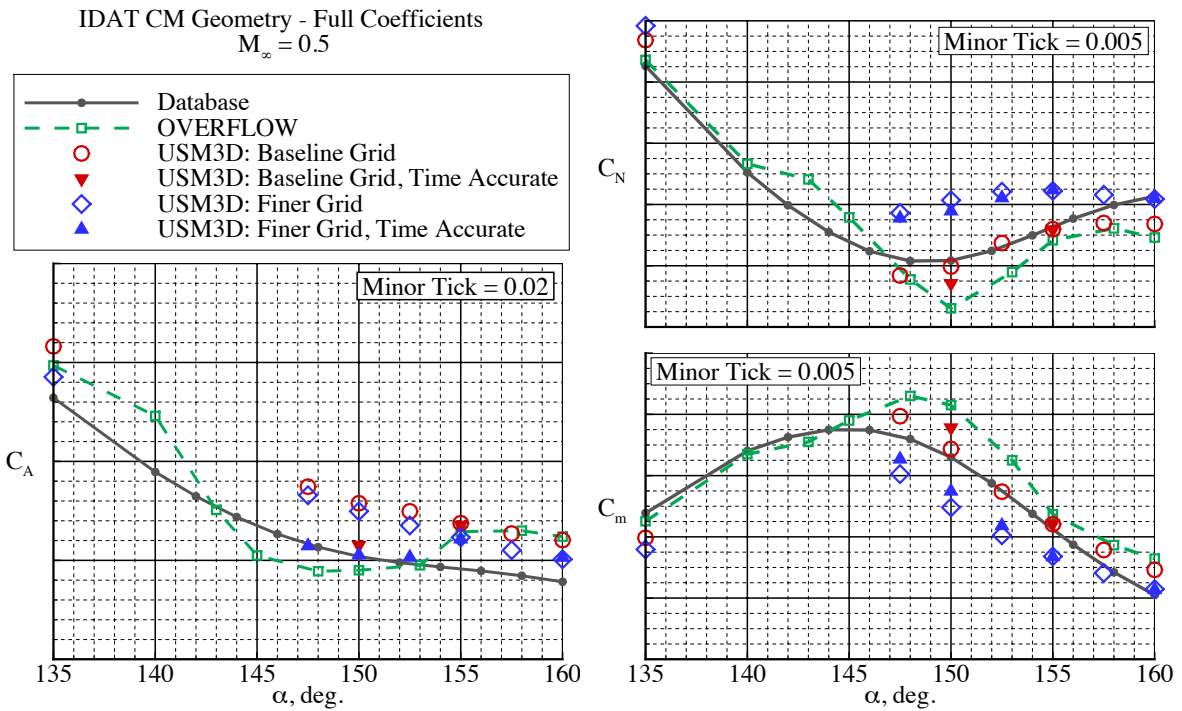


Figure 15. Base and adapted grids on the $\phi = 0^\circ$ plane for the IDAT CM configuration at $M_\infty = 0.5$ and $\alpha = 150^\circ$.



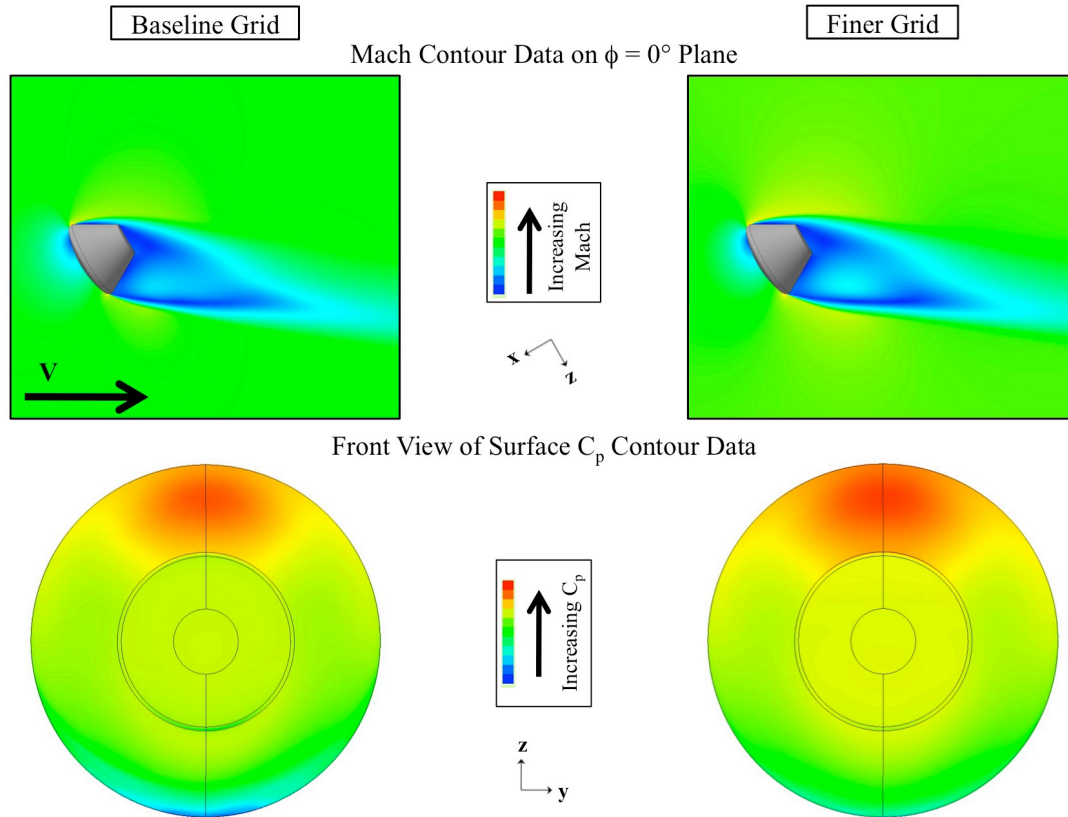


Figure 17. Mach and C_p contour data for the steady-state solutions on the IDAT CM configuration at $M_\infty = 0.5$ and $\alpha = 150^\circ$.

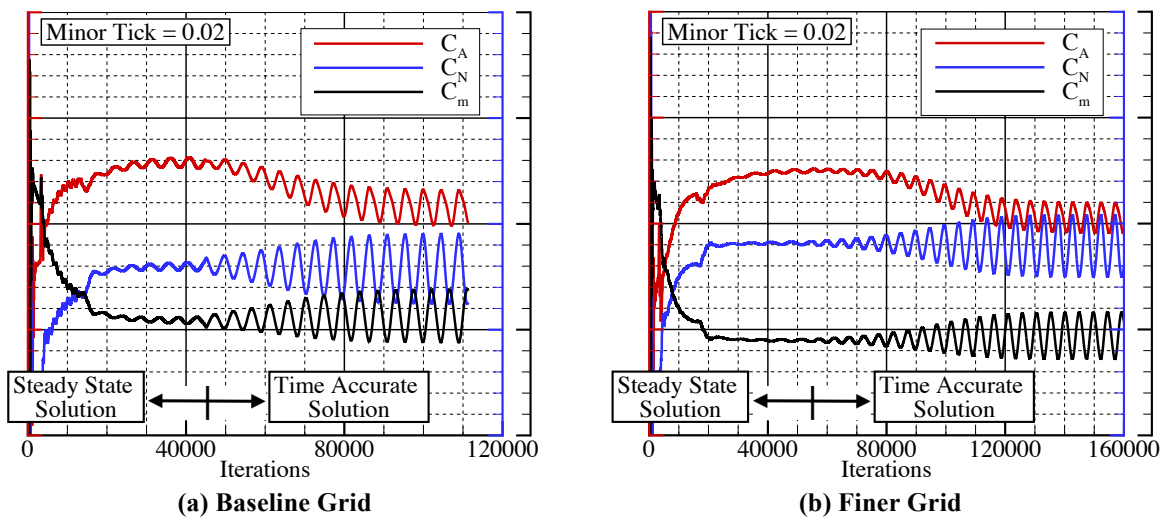
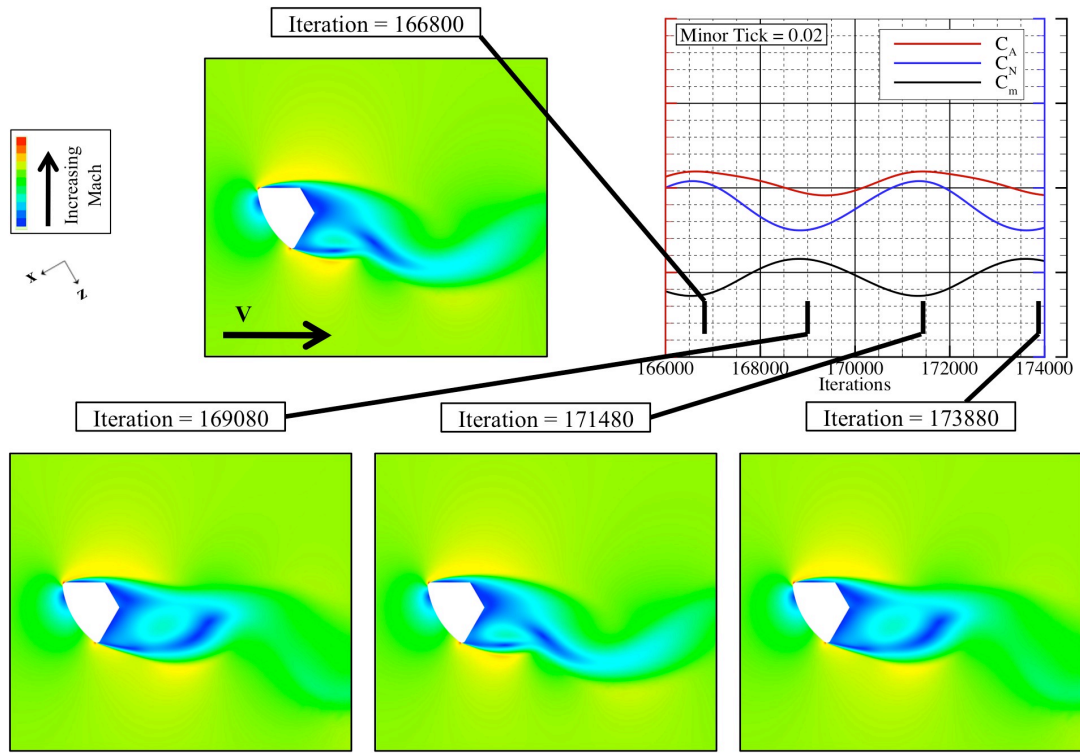
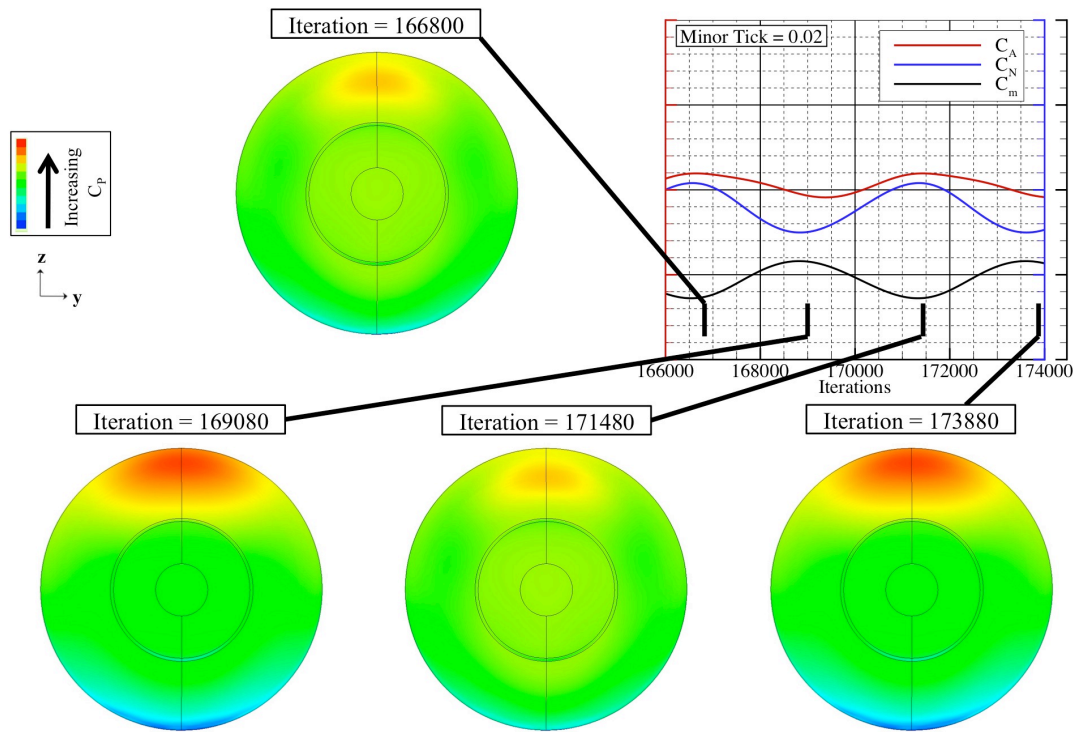


Figure 18. Coefficient convergence histories for time-accurate solutions on the IDAT CM configuration at $M_\infty = 0.5$ and $\alpha = 150^\circ$.



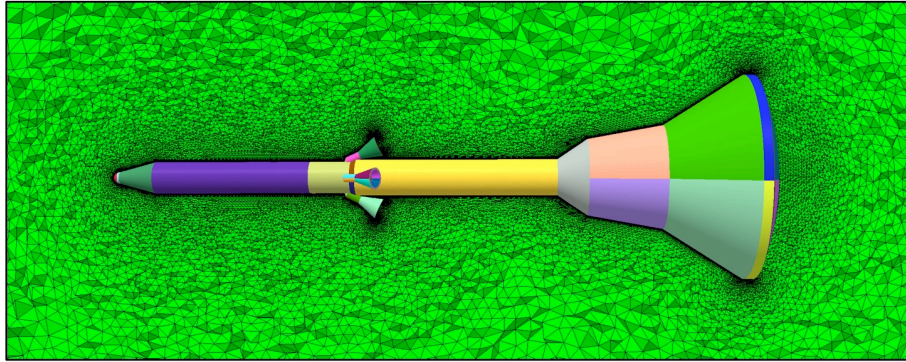
(a) Mach contour data on the $\phi = 0^\circ$ plane.



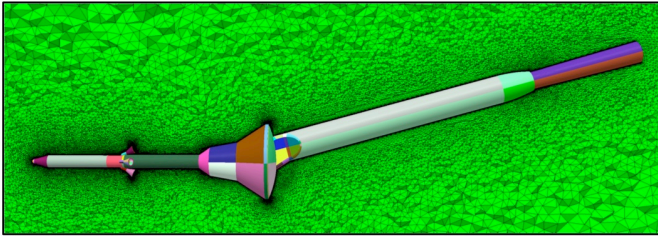
(b) Front view of the surface C_p contour data.

Figure 19. Mach and surface C_p contour data from the time-accurate solution on the finer grid for the IDAT CM configuration at $M_\infty = 0.5$ and $\alpha = 150^\circ$.

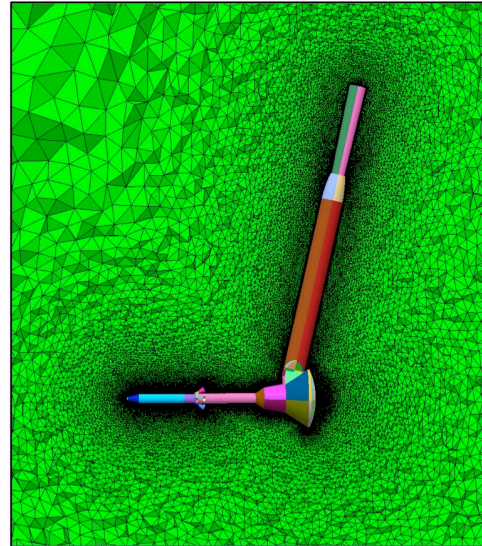
Free Air Configuration – $0^\circ \leq \alpha \leq 180^\circ$



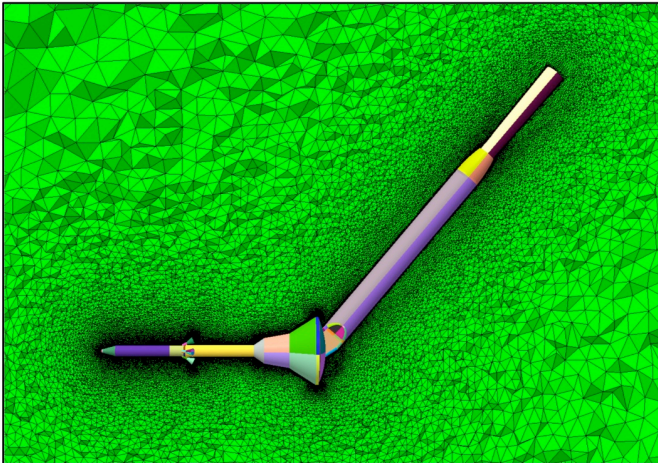
LAV with 15° Sting – $0^\circ \leq \alpha \leq 30^\circ$



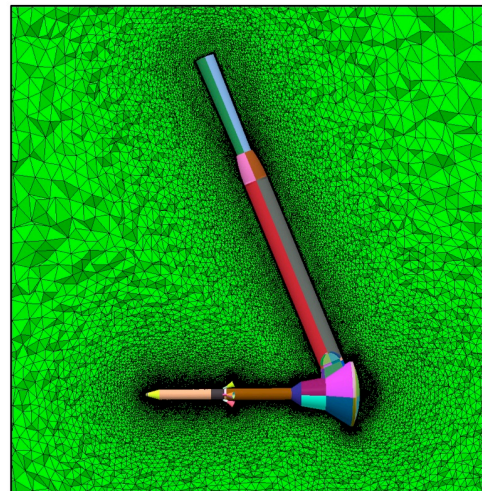
LAV with 77.5° Sting – $60^\circ \leq \alpha \leq 95^\circ$



LAV with 50° Sting – $30^\circ \leq \alpha \leq 70^\circ$



LAV with 11.5° Sting – $95^\circ \leq \alpha \leq 130^\circ$



LAV with 162.5° Sting – $150^\circ \leq \alpha \leq 180^\circ$

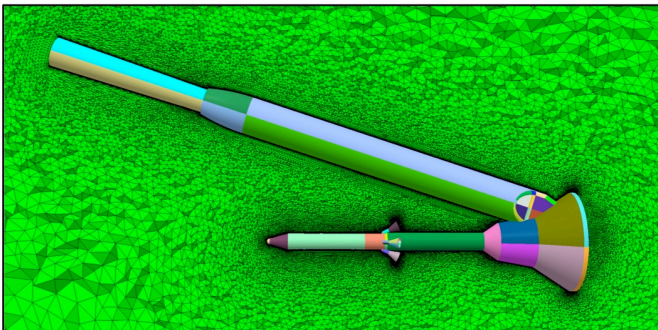


Figure 20 Grids and α -ranges for the different model/sting configurations of the 19-AA LAV wind tunnel model.

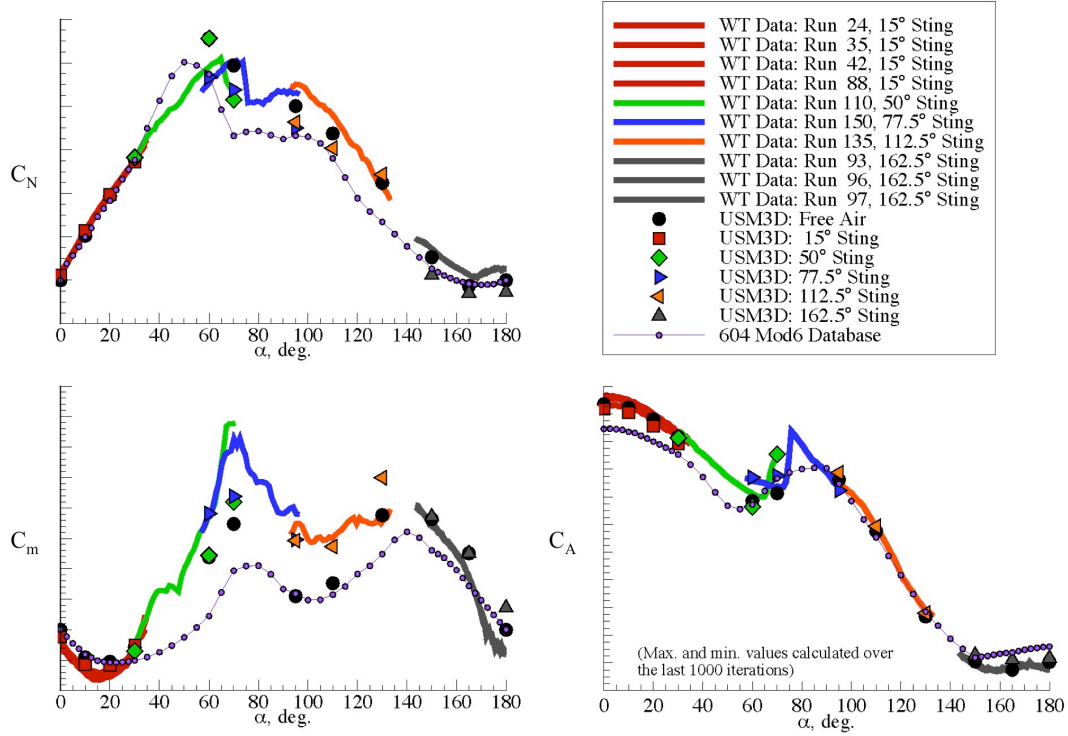


Figure 21. Comparison of USM3D, wind tunnel, and aero-database data for the 19-AA LAV wind tunnel model at $M_\infty = 0.9$ and $0^\circ \leq \alpha \leq 180^\circ$.

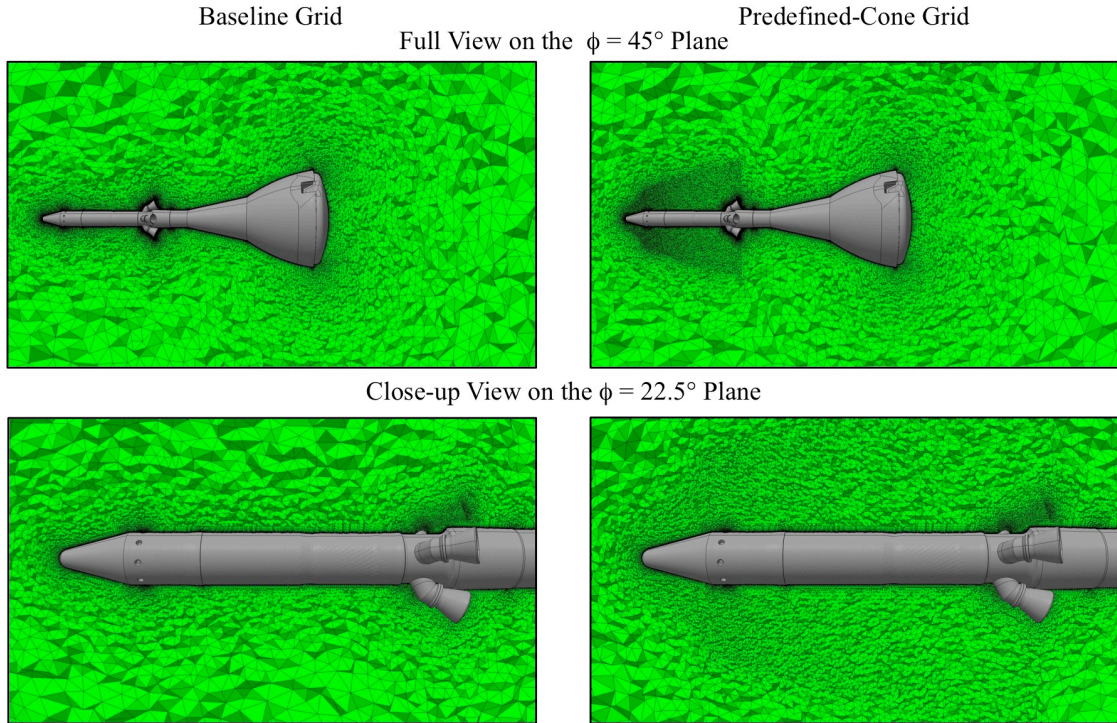
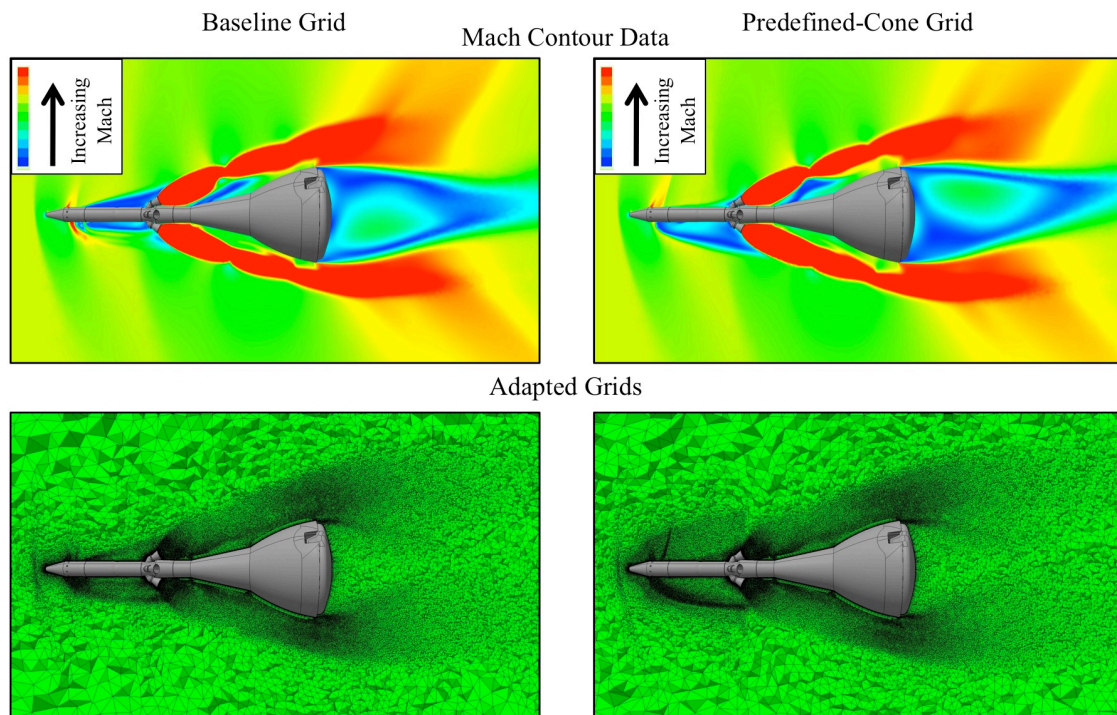
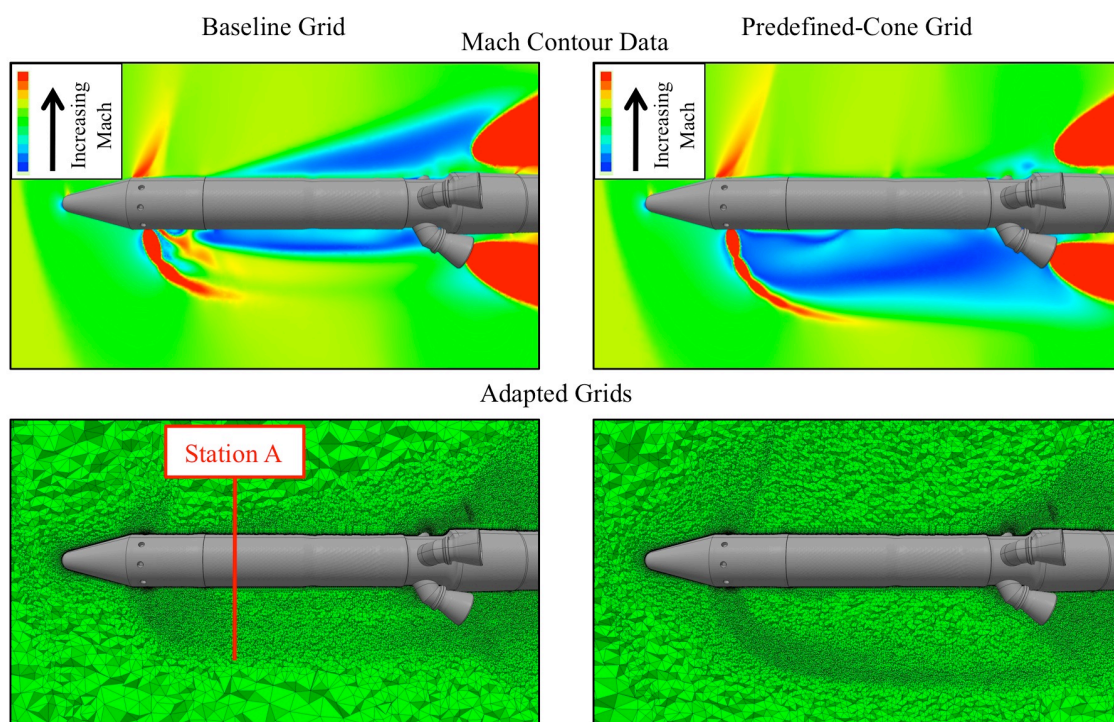


Figure 22. Cross-section views of the baseline and predefined-cone base grids for the 606F LAV configuration.

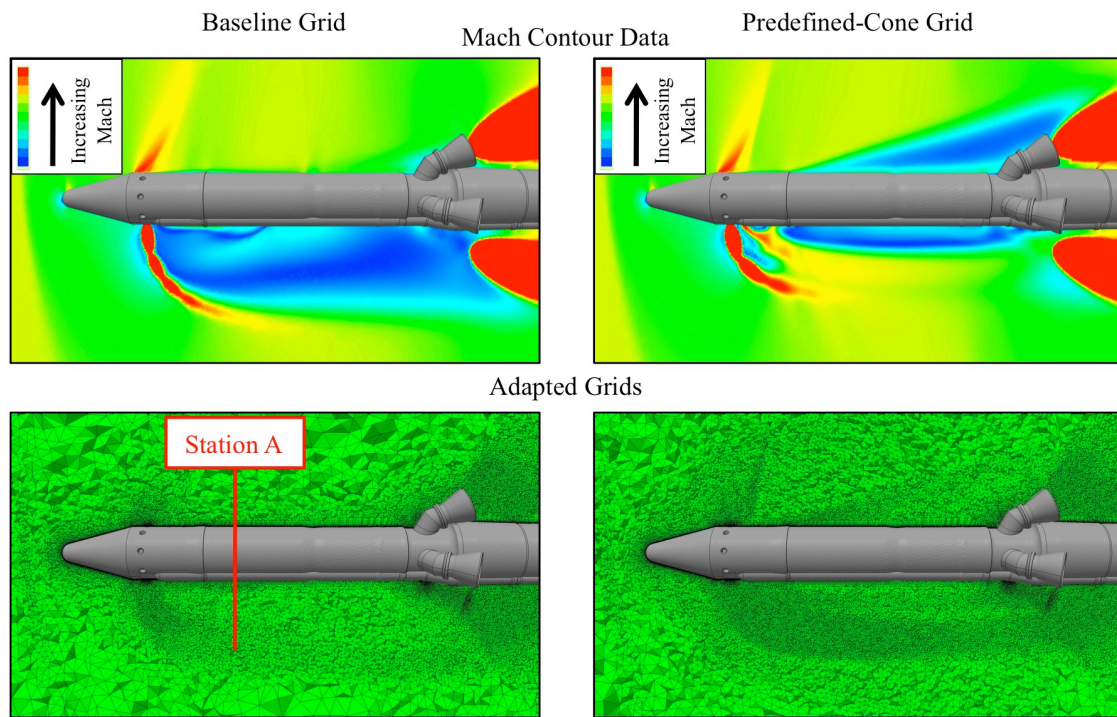


(a) Full view on the $\phi = 45^\circ$ plane.

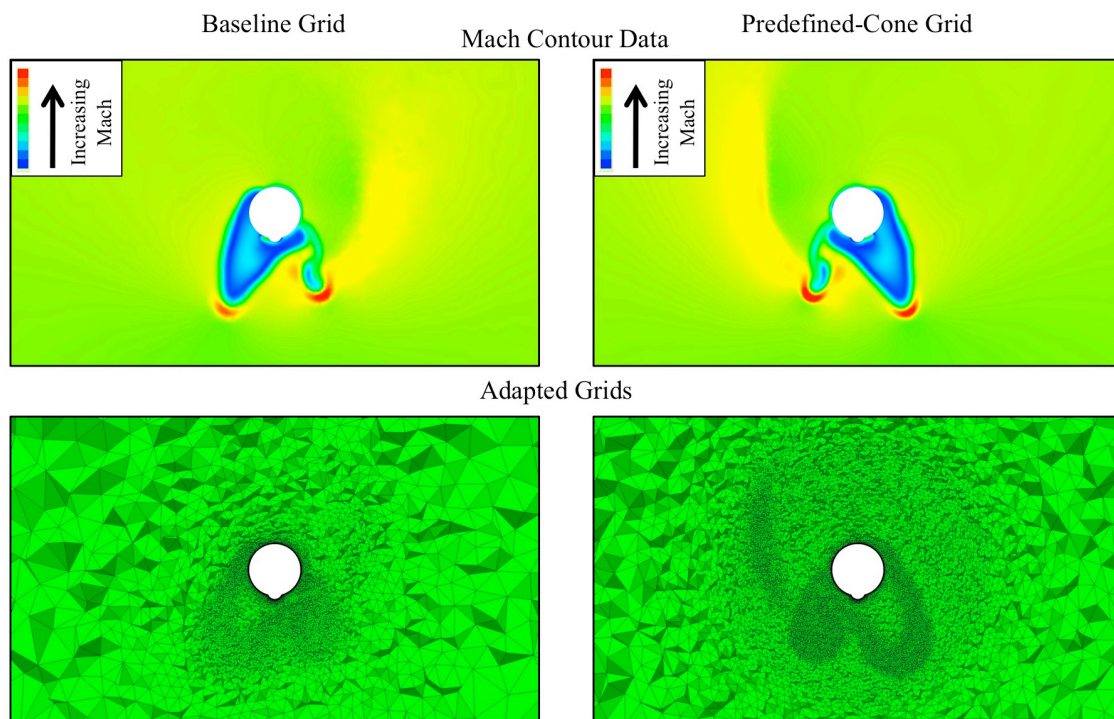


(b) Close-up view on the $\phi = 22.5^\circ$ plane.

Figure 23. Grids and Mach contour data at various cross-sections for the 606F LAV configuration at $M_\infty = 1.1$, $\alpha = 10^\circ$, $CT = 3.0$, and $TR = 0.04$.

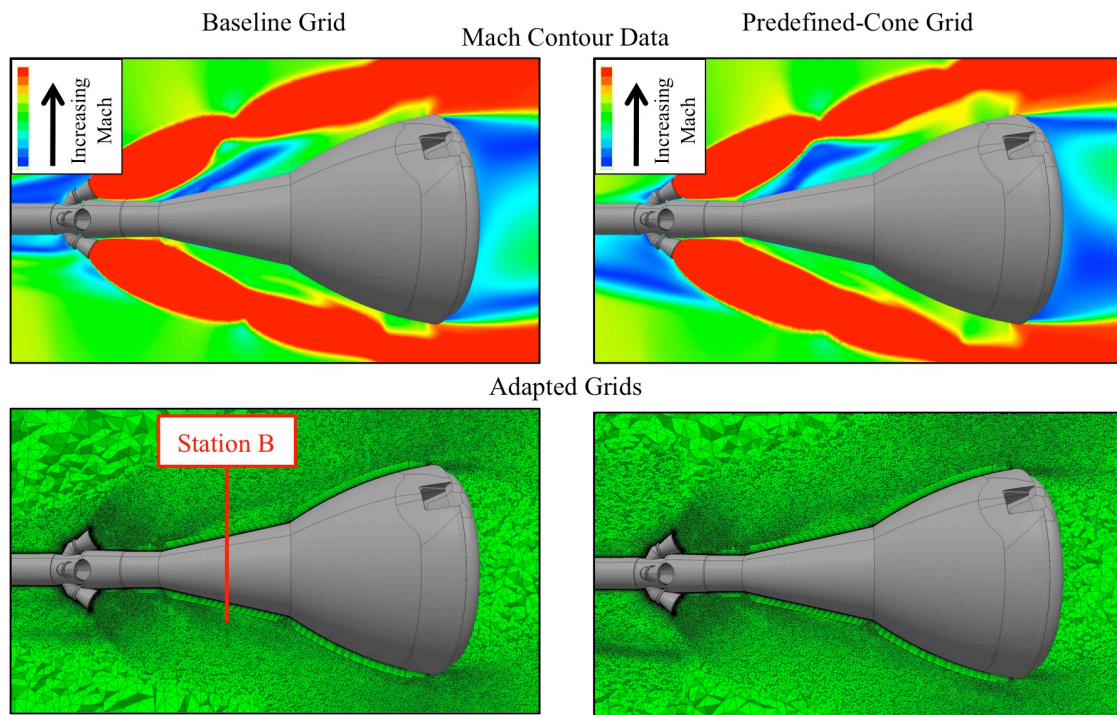


(c) Close-up view on the $\phi = -22.5^\circ$ plane.

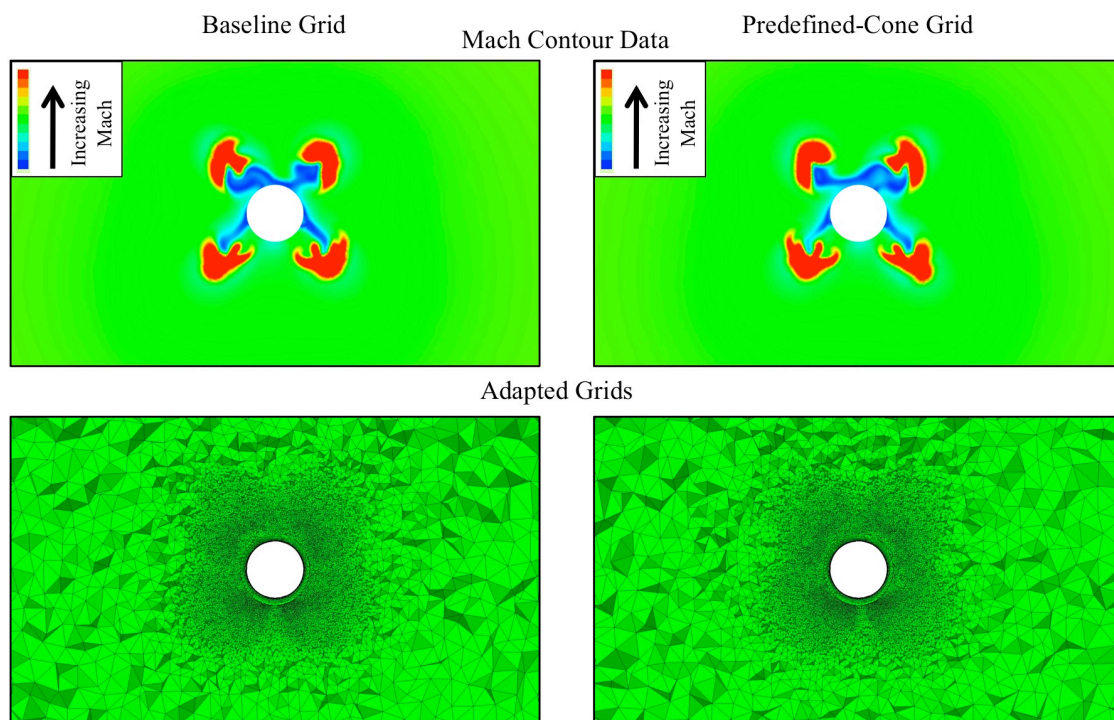


(d) View on the Station A plane.

Figure 23. Continued.



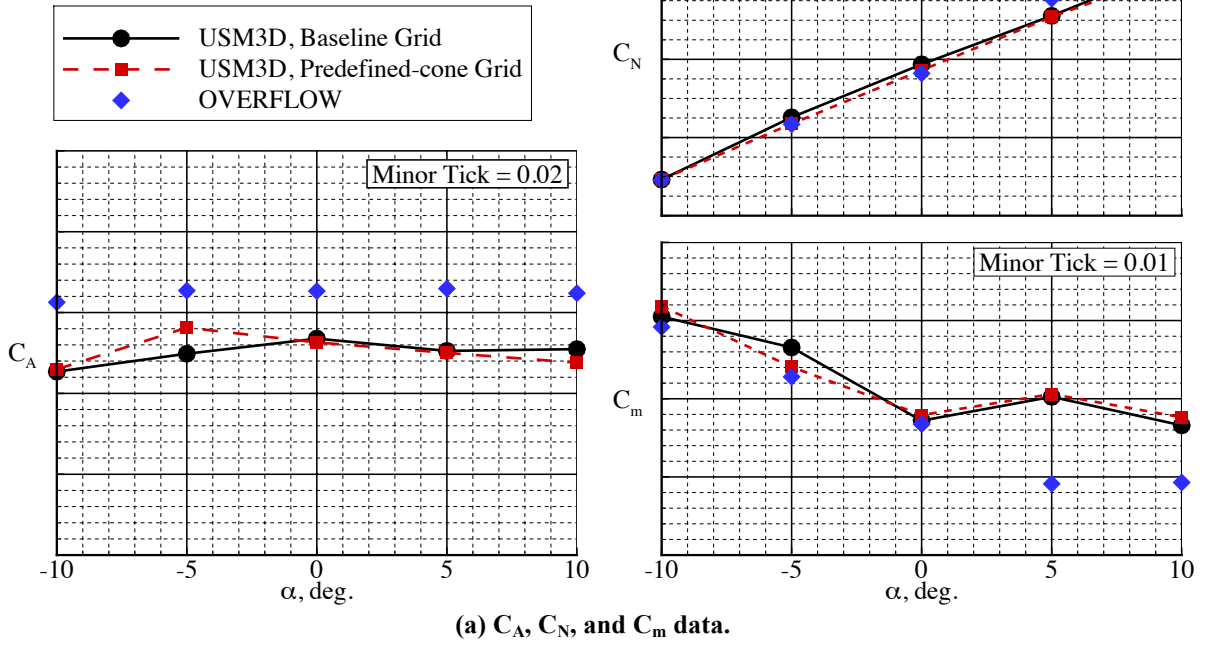
(e) Close-up view on the $\phi = 45^\circ$ plane.



(f) View on the Station B plane.

Figure 23. Concluded.

606F LAV Configuration - Full Coefficients
 $M_\infty = 1.1$, α Varies
 ACM TR = 0.04, AM CT = 3.0



606F LAV Configuration - Normalized Coefficients
 $M_\infty = 1.1$, α Varies
 ACM TR = 0.04, AM CT = 3.0

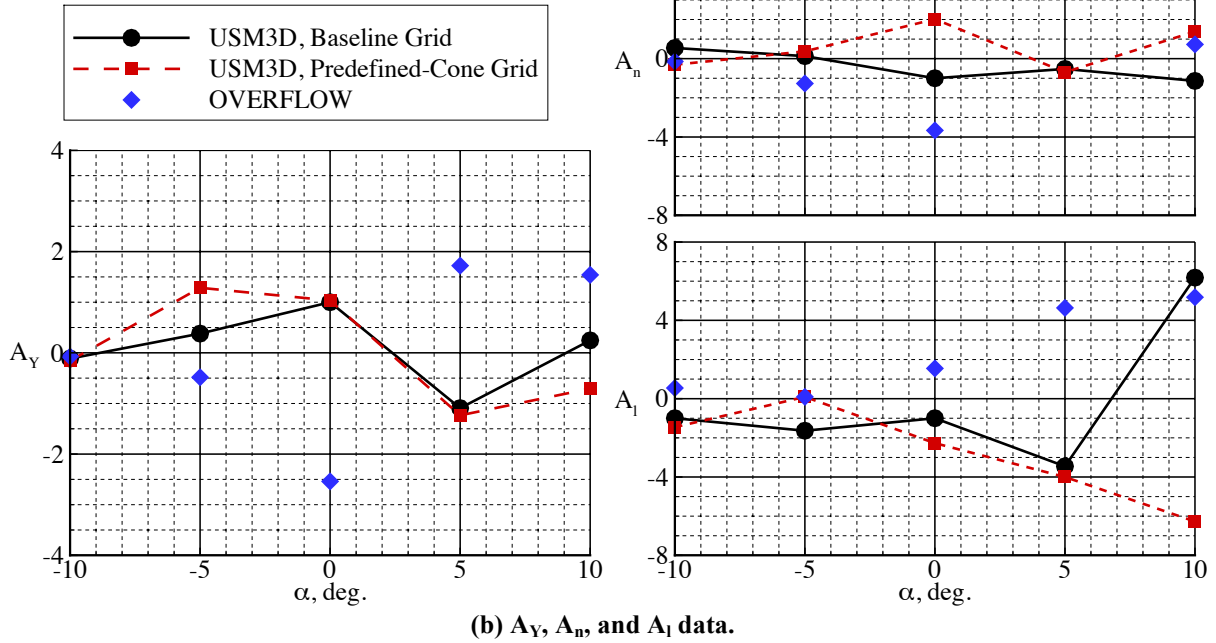


Figure 24. Comparison of USM3D and OVERFLOW data for the 606F LAV configuration at $M_\infty = 1.1$, $-10^\circ \leq \alpha \leq 10^\circ$, CT = 3.0, and TR = 0.04.

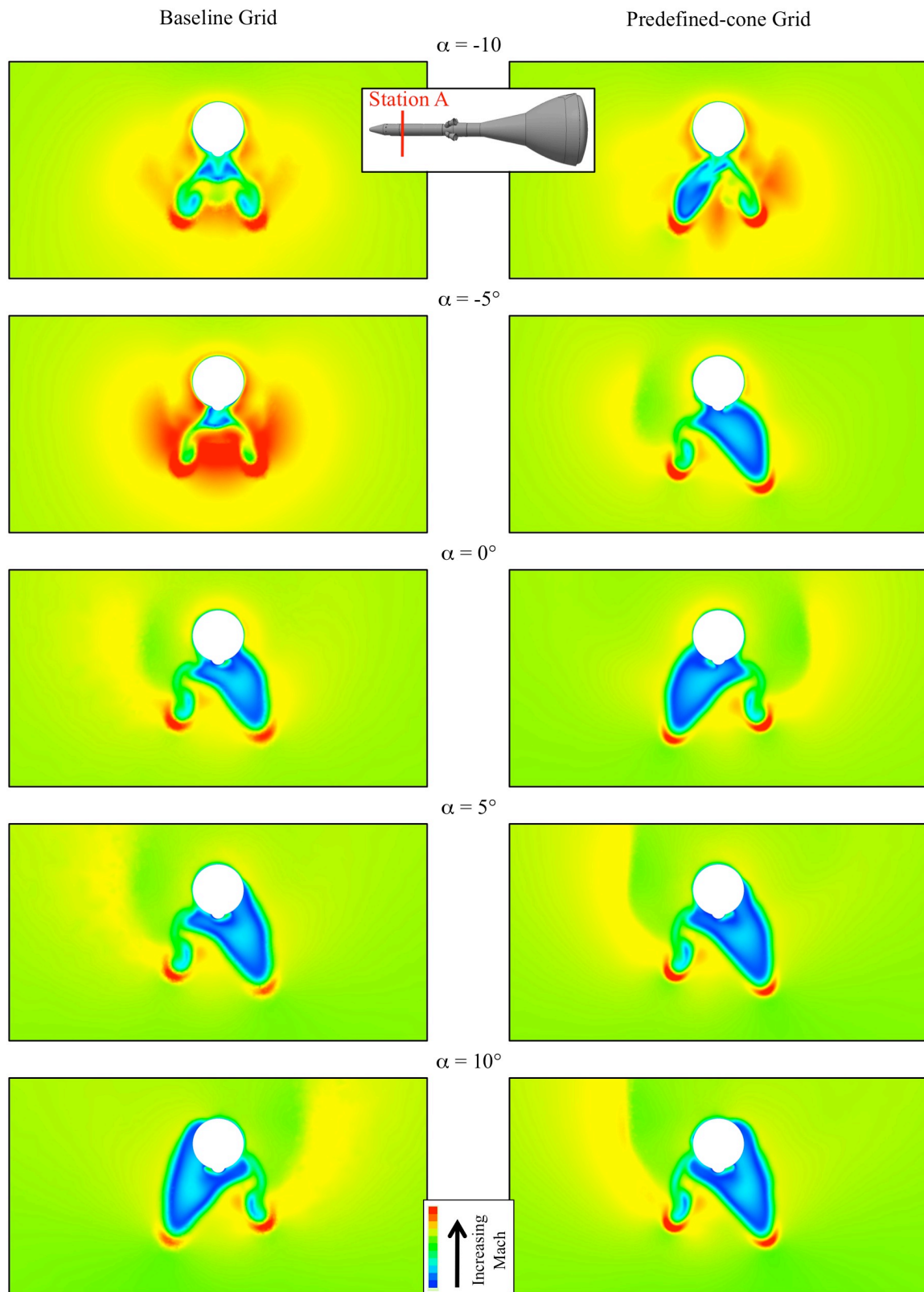


Figure 25. USM3D Mach contour data for two solutions on different grids at Station A on the 606F LAV configuration at $M_\infty = 1.1$, $-10^\circ \leq \alpha \leq 10^\circ$, $CT = 3.0$, and $TR = 0.04$.

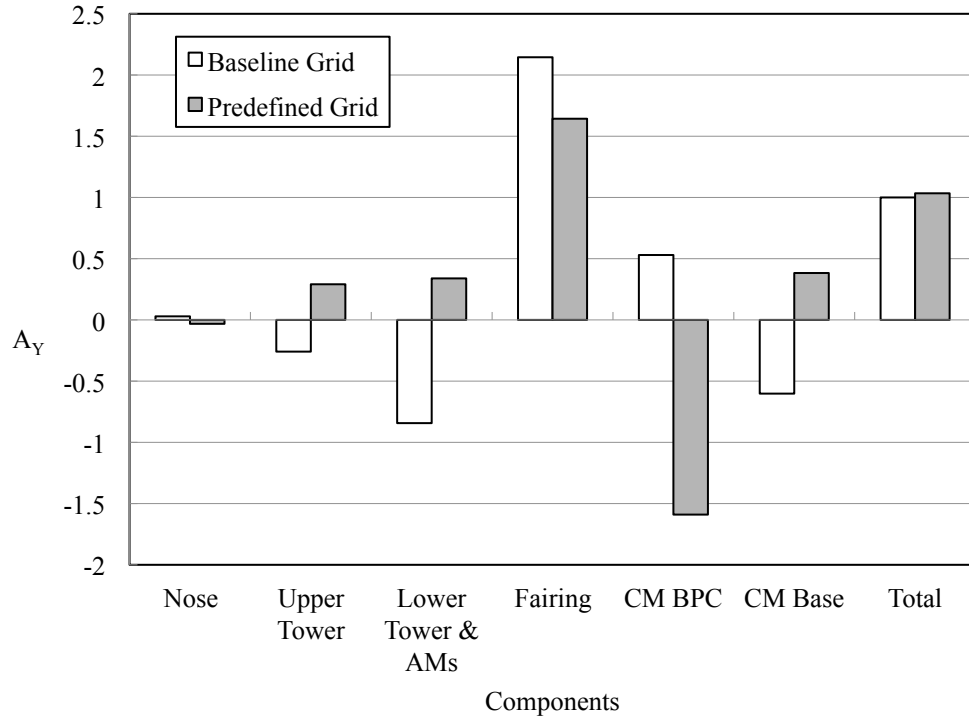
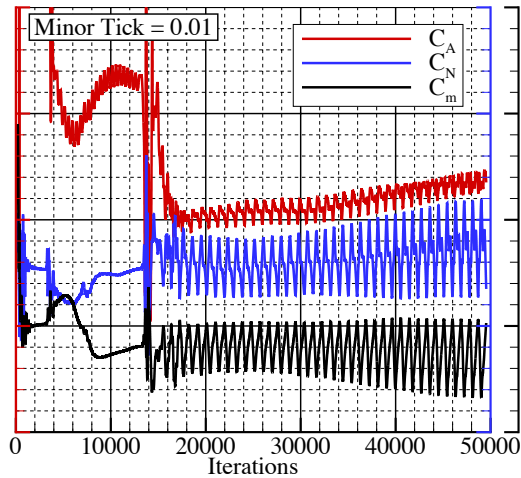
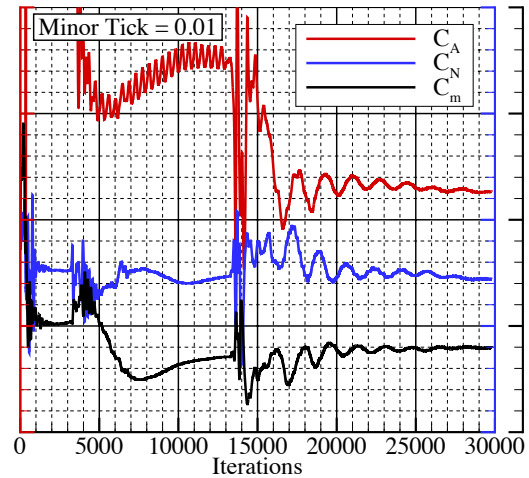


Figure 26. USM3D CA data for the total configuration and each component of the 606F LAV configuration at $M_\infty = 1.1$, $\alpha = 0.0^\circ$, $CT = 3.0$, and $TR = 0.04$.



(a) Baseline grid.



(b) Predefined-cone grid.

Figure 27. Convergence histories for the baseline and predefined-cone grids for the 606F LAV configuration at $M_\infty = 1.1$, $\alpha = 0.0^\circ$, $CT = 3.0$, and $TR = 0.04$.

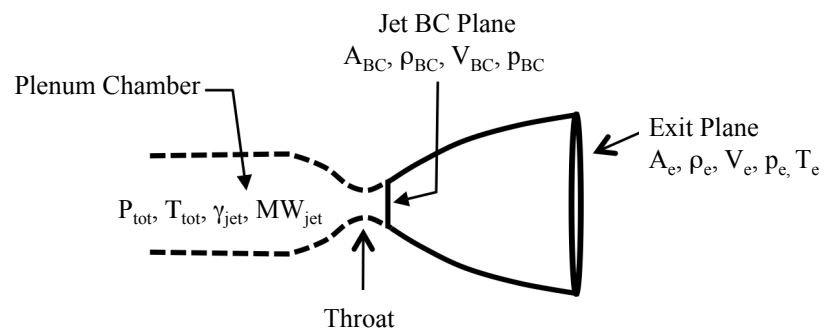


Figure A1. Schematic of nozzle jet boundary condition prescription.